# Chapter 7
# Modeling of Biomineralization and Structural Color Biomimetics by Controlled Colloidal Assembly

**Xiang Yang Liu and Ying Ying Diao**

**Abstract** This chapter aims to give an overview on the recent progress of the electrically controlled colloidal assembly, as an experimental modeling system to study the crystallization-related biomineralization processes. The controlled colloidal assembly allows us not only to visualize some "atomic" details of the nucleation and surface process of crystallization, but also to treat quantitatively the previous models to such an extent that has never been achieved before by other approaches. As such, the crystallization processes were quantitatively examined at the single particle level, and the related kinetics, i.e., the kinetics of nucleation, multistep crystallization, supersaturation-driven structural mismatch nucleation, etc., can be verified from the single particle level. The results acquired can transfer our knowledge on biomineralization to a new phase. Apart from the fundamental aspects, the controlled colloidal crystallization has been attracted significant attention in many applications. In this concern, the application of colloidal crystallization to the fabrication of photonic crystals and the biomimetics of natural structural colors will be discussed.

**Keywords** Biomineralization • Assembly of biominerals • Supersaturation • Nucleation • homogeneous nucleation • heterogeneous nucleation • Supersaturation-driven interfacial structural mismatch • Shadow effect • Colloidal assembly • Photonic crystal • Structural color • Biomimetics • Double reflection • Silk fabrics • Multistep crystallization

X.Y. Liu (✉)
College of Materials, Xiamen University, 422 Si Ming Nan Road, 361005 Xiamen, P.R. China
e-mail: phyliuxy@nus.edu.sg

Department of Physics and Department of Chemistry, Faculty of Science, National University of Singapore, 2 Science Drive 3 117542, Singapore

Y.Y. Diao
College of Materials, Xiamen University, 422 Si Ming Nan Road, 361005 Xiamen, P.R. China

X.Y. Liu (ed.), *Bioinspiration: From Nano to Micro Scales*, Biological and Medical Physics, Biomedical Engineering, DOI 10.1007/978-1-4614-5372-7_7,
© Springer Science+Business Media New York 2012

## 7.1 Introduction

Crystallization plays a crucial role in biomineralization, the preparation of functional materials [1–4], the structural characterization of natural and synthetic molecules [5, 6], and the development of advanced technologies [7, 8]. Nowadays, many nanomaterials are crystalline phases, and the essential structures and utmost important properties of the systems are determined by nucleation and the correlation between the nucleating nanophase and the substrate, etc. The control of crystallization is directly related to some soft materials and nanophase formation [9].

Up to now, crystallization is still considered as art other than science, mainly because there is not sufficient knowledge on its critical early stages and the atomic processes. In this regard, the kinetics of the transition from the metastable structure to the stable structure has so far been open to question. The key challenge is the in situ imaging of the atomic/molecular dynamic process, which is limited by both the spatial and the temporal definitions of current technologies and the absence of the direct observation on the transition process in real space, except for some local events of crystallization/quasicrystallization of large species, namely proteins [10] and colloidal particles [11]. Notice that computer simulations have been applied to acquire the information [12]. Nevertheless, due to the constraint of computation power and the methodologies, the knowledge obtained is still limited. It is therefore of critical importance to develop a new methodology to "simulate" or "monitor" the atomic/molecular dynamic process of the nucleation and growth of crystals [13].

Colloids, the dispersions of nano/microsized particles in a fluid background solvent, range from ink, milk, mayonnaise, paint, and smoke and have many practical applications [14–16]. Nowadays, colloids have been employed as a model system to study phase transitions [17–22]. In this regard, these nano/microsized colloids provide an important platform for sampling the aggregation and assembly at the single particle level because of its visible size, tractable dynamics, and tunable interparticle interactions [12–16, 23–25]. In addition, colloidal particles in solutions behave like big "atoms" [19, 20], and the phase behavior of colloidal suspensions is similar to that of atomic and molecular systems [21]. Therefore, from the point of view of crystallization modeling, the growth units are colloidal particles, and thus the crystallization process can be observed directly by a normal optical microscope. Furthermore, the interaction among colloidal particles can be turned by the adjustment of the ionic strength, pH of solutions/suspensions, and the applied electric field strength and frequency; therefore, the thermodynamic driving force for the crystallization can be controlled precisely in such a system. This allows the quantitative measurement and the data interpretation similar to computer experiments [20, 21]. Besides, proteins and viruses are in the colloidal domain. Any advantage in the understanding of colloidal crystallization will exert a direct impact on the control of proteins and biomacromolecule crystallization. Apart from modeling, from the technological point of view, the knowledge of nucleation, growth, and defect generation is very important in identifying robust technologies in electronic, photonic, and life sciences and technologies.

In practice, controlling the colloidal assembly could be employed to define a template for creating two-dimensional (2D)/three-dimensional (3D) periodic structures for applications in photonic devices [26, 27], biological and chemical sensors [28], and tunable lasers [29]. Recently, the controlled colloidal assembly has been utilized to mimic the structural color created by animals, i.e., butterfly wings, etc. [30, 31].

The purpose of this chapter is to provide an overview on the recent progress in the experimental simulations of crystallization processes, in particular biomineralization processes, by controlled colloidal assembly. Our attention will be focused on the following two aspects: the electrically controlled colloidal crystallization as a well-controlled and quantitative modeling system to simulate the kinetics of crystallization, i.e., biomineralization, and structural color biomimetics. As the thermodynamic driving force in crystallization can be tuned directly from altering the strength and/or frequency of the applied electric field, some most essential issues in biomineralization, i.e., nucleation kinetics, the multistep/phase crystallization, the ordered crystallites assembly, etc., which are often observed in hard tissues, can be examined quantitatively by the electrically controlled colloidal assembly in a combination of microscopic visualization. The results obtained will provide the most up-to-date knowledge on crystallization at the individual growth unit level. On the other hand, we will also review that, practically, the controlled colloidal assembly can be adopted to produce templates in engineering photonic crystals in mimicking structural colors from the animal kingdom. In this regard, some examples of structural color biomimetics and the application to textiles will be given. This may pave the new silk road in the years to come.

## 7.2 Thermodynamic Driving Force of Colloidal Crystallization and Assembly

As crystallization in most cases is a first-order phase transition, without thermodynamic driving force, crystallization (including biomineralization) will not take place. Therefore, to examine the kinetics of crystallization (including biomineralization) in a quantitative way, the well-controlled thermodynamic driving force is the precondition. Furthermore, exercising the control of crystallization should demonstrate the capability of controlling the thermodynamic driving force for the theoretical analysis. Regarding the colloidal crystallization, the interactions among colloidal particles play a key role in this analysis. The most general equation of the total free-energy difference ($\Delta G$) between particles at a separation $H$ is obtained by adding these contributions:

$$\Delta G = \Delta G^{\mathrm{att}}(\mathrm{vanderWaals}) + \Delta G^{\mathrm{rep}}(\mathrm{shortrange}) + \Delta G^{\mathrm{rep}}(\mathrm{electrostatic}) + \Delta G^{\mathrm{rep}}(\mathrm{steric}) + \Delta G(\mathrm{othereffects}) \tag{7.1}$$

where superscripts "att" and "rep" denote attraction and repulsion respectively. The consideration for the overall interactions mentioned above has been treated by the Deryagin–Landau–Verwey–Overbeek theory [32]. In practice, it is not necessary to consider all these contributions simultaneously. One shall here deal with *two simpler situations* where the long-range potential arises from electrostatic *and/or* from steric repulsion contributions. Notice that the double-layer repulsion depends on the ionic strength of the medium: the curves may show a high repulsive barrier at low ionic strengths, a so-called secondary minimum at intermediate ionic strengths, and a negligibly small barrier, or none at all, at higher ionic strengths. In the same way, the form of the steric repulsion is determined by the nature of the interactions between the adsorbed polymer chains and the solvent. A repulsive barrier of variable range and a minimum of variable depth can result, depending on the solvent and the temperature. The interaction between colloidal particles can be turned by changing the ionic strength, pH of solutions, or adding polymers. This implies that the "phase behavior" of such systems can be tuned by altering the above parameters.

Apart from the above-mentioned forces, the recent researches indicate that the interaction between colloidal particles can be induced and controlled by an alternating electric field (AEF) [13, 31, 33–46]. One can tune the interaction by altering the frequency and/or the strength of the applied field. This effect can be captured by $\Delta G$(other effects) in (7.1). In comparison with other stimuli, the electric stimulus can be applied and switched off instantly without disturbing the original solutions. Although the interactions between colloidal particles can be of many kinds, they are basically functions of $1/r_{eq}$ ($r_{eq}$ denotes the equilibrium distance between two neighboring particles). This implies that for a given colloidal system, the interaction between two adjacent particles is fixed once $r_{eq}$ is constant. In other words, the change of $r_{eq}$ can reflect directly the change of interparticle interactions.

As tuning the frequency and field strength of an AC field is much easier to achieve than other means, the following discussion will be mainly focused on the control of the colloidal crystallization under an AC field (i.e., Fig. 7.1) [35, 37, 39]. Nevertheless, not all ranges of frequency and intensity of the AC field can produce a crystalline assembly of particles. There exists a finite frequency range with well-defined lower and upper cut-off values of particle size, charge, ionic strength of the solution, pH, etc., in which the effective control can be implemented (i.e., Fig. 7.1).

The formation of various patterns is subject to the balance of the attractive and repulsive forces. Here, the attractive force that can overcome the interparticle electrostatic repulsion and enable 2D colloidal aggregation is suggested to be attributed to electrohydrodynamic flow [47, 48]. Fluid motion is set up by the interaction between this free charge and the lateral electric field, which is caused by the distortion of the applied field by the colloidal particles. A "phase diagram" of the electrically controlled colloidal assembly under a constant temperature is given in Fig. 7.1.

The thermodynamic driving force for the phase transition (including biomineralization and general crystallization) can be defined by $\Delta\mu$, referring to the difference

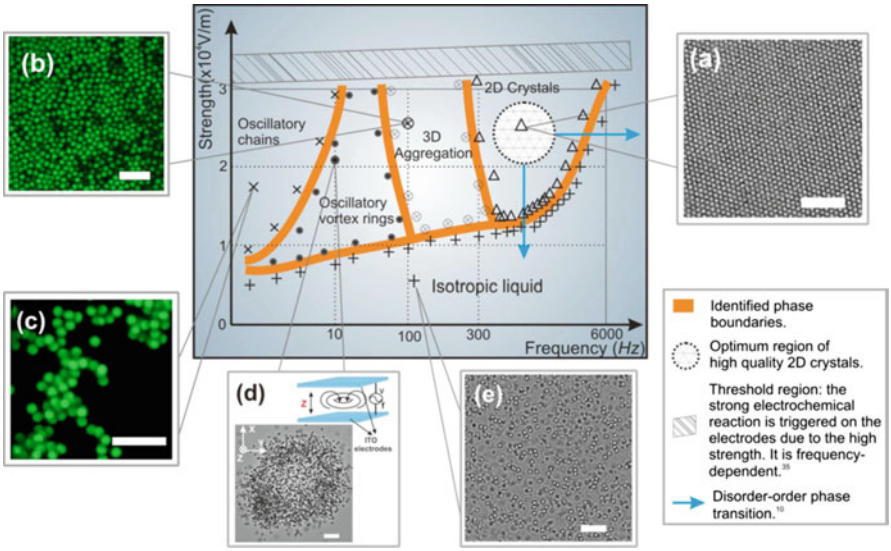


**Fig. 7.1** The diagram of electrically controlled colloidal assembly. The phase diagram and typical colloidal patterns induced by an AEF at room temperature. (**a**) A 2D colloidal crystal at field strength $\sigma_E = 2.6\times10^4$ V/m and $f = 800$ Hz. (**b**) 3D aggregation of colloidal particles, as captured by the LCSM at $\sigma_E = 2.4\times10^4$ V/m and $f = 100$ Hz. (**c**) Static snapshot of colloidal chains by the LCSM at $\sigma_E = 1.8\times10^4$ V/m and $f = 0.1$ Hz. (**d**) Snapshot of oscillatory vortex rings at $2.3\times10^4$ V/m and $f = 1$ Hz. (**e**) The isotropic liquid state of colloidal suspension. Scale bars in (**b**) and (**c**) represent 5 μm, and in (**a**), (**d**), and (**e**) represent 10 μm. Colloidal suspension (0.1% in volume fraction) of monodisperse charged polystyrene spheres (1 μm in diameter) is confined to a horizontal layer between two conductive glass microscope slides. Glass spacers set the layer thickness in the cells at $2H = 120 \pm 5$ μm across the 1.5 cm × 1.5 cm observation area. The AEF was supplied by a waveform generator. The motions of the colloidal particles are recorded with a computer-driven digital CCD camera. Reprinted with permission from Ref. [45] ©2009 American Institute of Physics

between the chemical potentials of a growth unit in the ambient phase $\mu_i^{\text{ambient}}$ and in the crystalline phase $\mu_{\text{crystal}}$:

$$\Delta\mu = \mu_i{}^{\text{ambient}} - \mu_{\text{crystal}} \tag{7.2}$$

where subscript $i$ denotes the solute in the ambient phase. When $\Delta\mu > 0$, the system is said to be supersaturated. This is the thermodynamic precondition for crystallization. Conversely, when $\Delta\mu < 0$, the system is undersaturated. Under such a condition, crystals will dissolve. When $\Delta\mu = 0$, the ambient phase is in equilibrium with the crystalline phase. As for temperature $T$ and pressure $P$, one has $(\mu_i^{\text{ambient}})_{\text{eq}} = \mu_{\text{crystal}}$, where $(\mu_i^{\text{ambient}})_{\text{eq}}$ is the chemical potential of a solute molecule in a state of phase equilibrium. Then for crystallization from solutions, the chemical potential of species $i$ is given by [49, 50]

$$\mu_i = \mu_i^0 + kT \ln a_i \approx \mu_i^0 + kT \ln C_i \tag{7.3}$$

where $a_i$, and $C_i$ denote the activity and concentration of species $i$, respectively, and $\mu_i^0$ denotes the standard state ($a_i = 1$) of the chemical potential of species $i$. This then gives rise to the thermodynamic driving force

$$\frac{\Delta\mu}{kT} = \ln\frac{a_i}{a_i^{\mathrm{eq}}} \approx \ln\frac{C_i}{C_i^{\mathrm{eq}}} \tag{7.4}$$

where $a_i^{\mathrm{eq}}, C_i^{\mathrm{eq}}$ are, respectively, the equilibrium activity and concentration of species $i$. If we define the supersaturation for crystallization as

$$\sigma = (a_i - a_i^{\mathrm{eq}})/a_i^{\mathrm{eq}} \approx (C_i - C_i^{\mathrm{eq}})/C_i^{\mathrm{eq}} \tag{7.5}$$

(7.4) can then be rewritten as

$$\frac{\Delta\mu}{kT} = \ln(1+\sigma) \cong \sigma(\text{if } \sigma << 1) \tag{7.6}$$

For colloidal crystallization, the similar relationship can be found. If the interaction between the particles in the crystal phase remains constant at different field strength and frequencies, the supersaturation can be given by (7.6) $\sigma = (\phi - \phi_m)/\phi_m$ ($\phi$ and $\phi_m$ represent the actual concentration and the equilibrium concentration of the solute, respectively). For more precise definition of supersaturation in biomineralization, refer to Chap. 3.

## 7.3 Simulations of Nucleation and Crystal Growth in Biomineralization

Similar to the crystallization of other materials, 3D crystallization of biominerals occurs via (1) *the nucleation*, followed by (2) *the growth* of crystals. Nucleation will determine whether and when a mineral (crystalline) phase will occur and the correlation with its surroundings. It will also determine the total number and the average size of crystalline particles occurring in the system eventually. On the other hand, the growth of crystals will to a large extent determine the size, morphology, and perfection of crystals. Therefore, the understanding of the governing mechanism will allow us to acquire the knowledge on how organisms can exercise the effective control and on the engineering of biomineral crystalline materials. In this regard, how the colloidal crystallization can be controlled electrically can be applied to model the general process of nucleation and biomineralization-related phenomena, i.e., multistep/phase crystallization, anti-templating effect, etc.

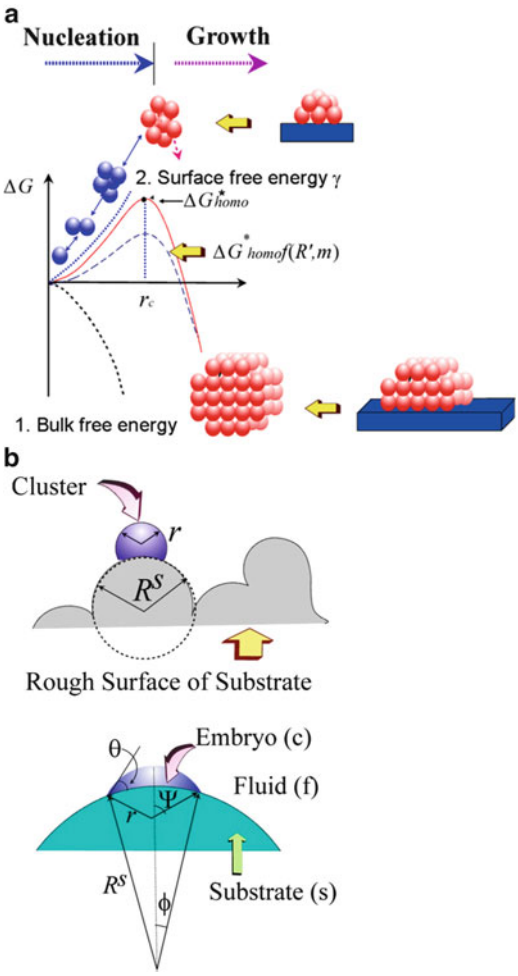


**Fig. 7.2** (**a**) Crystallization normally takes place via nucleation, followed by the growth of crystals. Nucleation is a kinetic process of overcoming the nucleation barrier, which is the outcome of the occurrence of the surface free energy $\gamma$. (**b**) Illustration of nucleation on a rough substrate. Reprinted with permission from Ref. [9], ©2004 Springer

### *7.3.1 Nucleation Barrier*

Nucleation can be regarded as a process of creating "baby crystallites" in the mother (or ambient) phase. The key step is to overcome a so-called nucleation barrier in the clustering process, which determines the rate of generating "mature" crystals in the unit volume of the ambient phase. Under the condition of crystallization, the crystal phase is the thermodynamically stable phase. As shown in Fig. 7.2, the occurrence of nucleation barrier is subject to the occurrence of the interfacial energy between the crystal phase and the ambient phase. In other words, if there is no interfacial energy between the ambient and the crystal phases, there will not be any nucleation barrier.

During nucleation, if the probability of creating critical nuclei is uniform throughout the system, nucleation is defined as *homogeneous nucleation*. Otherwise, it is defined as *heterogeneous nucleation*. Notice that what has been mentioned above is normally referred to as 3D nucleation. During crystal growth, the so-called 2D nucleation will take place at the growing crystal surfaces in order to create new growing layers. When the growth of a crystal surface occurs under its critical roughening temperature, there will be a non-zero free energy in correspondence to the interfacial free energy in 3D. The so-called step free energy is associated with the creation of a step of unit length at the surface. Such a crystal face has atomically a smooth surface. Due to the step free energy, the creation of a new layer on the existing layer of the crystal surface should overcome a free energy barrier, similar to 3D nucleation barrier. If the crystals are free of screw or mixed dislocations, they grow by the mechanism of 2D nucleation [16] and the growth rate $R_g$ is largely determined by the 2D nucleation rate. Although they are not exactly the same, both 3D and 2D nucleation share many common features in almost all aspects [50, 51] Therefore, the analysis on 2D nucleation can be applicable to 3D nucleation, and vice versa.

As one of the most important factors, the nucleation rate $J$ is determined by the height of the free energy barrier, the so-called nucleation barrier. The free energy change associated with the formation of a cluster of molecules can be found from thermodynamic considerations, since it is defined as

$$\Delta G = G_{\text{fin}} - G_{\text{ini}} \tag{7.7}$$

for a system at constant pressure and temperature ($G_{\text{ini}}$ and $G_{\text{fin}}$ denotes the Gibbs free energies of the system in the initial and final states before and after cluster formation, respectively). If $M$ is the number of solute molecules in the system, one has then

$$\Delta G = -n\Delta\mu + \Phi_n \tag{7.8}$$

where $\Phi_n$ is the total surface energy of the $n$-sized cluster (except for the nucleation of bubbles when $\Phi_n$ contains also pressure–volume terms).The function $\Delta G$ reaches its maximum $\Delta G^*$ at $r = r_c$ or $n = n^*$ ($r$ and $r_c$ are the radius and the critical radius of the cluster, respectively). A cluster of $n^*$ molecules is a critical nucleus, $r_c$ is the radius of curvature of that critical nucleus, and $\Delta G^*$ is the nucleation barrier.

The occurrence of a foreign body in the system normally reduces the interfacial (or surface) free energy between the substrate and the nucleating phase; it will then lower the nucleation barrier according to (7.8). Given $\Delta G^*_{\text{homo}}$, the homogeneous nucleation barrier, and $\Delta G^*_{\text{heter}}$, the heterogeneous nucleation barrier, we can define an interfacial correlation factor $f$, describing the reduction of the nucleation barrier due to the occurrence of foreign body as

$$f = \frac{\Delta G^*_{\text{heter}}}{\Delta G^*_{\text{homo}}} \tag{7.9}$$

As shown in Fig. 7.2b, we assume that nucleation occurs on a rough substrate or foreign body with a radius of curvature $R^{\text{s}}$. The fluid phase is denoted by the subscript $f$, the crystalline phase by c, and the foreign body by s. If we denote the volume by $V$ and the surface area of the foreign body by $S$, then the free energy of formation of a cluster of radius $r$ on a foreign particle of radius $R^{\text{s}}$ is given, according to (7.8), by

$$\Delta G = -\frac{\Delta\mu V_{\text{c}}}{\Omega} + \gamma_{\text{cf}} S_{\text{cf}} + (\gamma_{\text{sf}} - \gamma_{\text{sc}}) S_{\text{sc}} \tag{7.10}$$

where $\gamma_{ij}$ is the surface free energy between phases $i$ and $j$, and $\Omega$ is the volume per structural unit. We have then

$$m = \frac{(\gamma_{\text{sf}} - \gamma_{\text{sc}})}{\gamma_{\text{cf}}} \approx \cos\theta \quad (-1 \leqslant m \leqslant 1) \tag{7.11}$$

To evaluate the critical free energy $\Delta G^*_{\text{heter}}$, we can substitute (7.11) and the expressions of $V_{\text{c}}$, $S_{\text{cf}}$, and $S_{\text{sc}}$ into (7.10) and require that

$$\frac{\partial \Delta G}{\partial r} = 0 \tag{7.12}$$

Solving (7.12) should, in principle, give the value of the critical radius. Nevertheless, it will involve a complicated and tedious treatment. On the other hand, a much simpler approach based on the thermodynamics principles can be adopted: it is known that a critical nucleus is a stable nucleus with the maximum curvature for a given thermodynamic condition. Under such an experimental condition, the size of the critical nucleus is the same for homogeneous and heterogeneous nucleation due to the Gibbs–Thomson effect [52–55]. We have then [54, 56] the radius of critical nuclei,

$$r_{\text{c}} = \frac{2\Omega\gamma_{\text{cf}}}{\Delta\mu} \tag{7.13}$$

Referring to Fig. 7.2c and taking

$$R' = \frac{R^{\text{s}}}{r_{\text{c}}} = \frac{R^{\text{s}}\Delta\mu}{\Omega\gamma_{\text{cf}}} = \frac{R^{\text{s}} kT \ln(1+\sigma)}{\Omega\gamma_{\text{cf}}}, \tag{7.14}$$

the free energy of formation of a critical nucleus is given according to (7.9) by

$$\Delta G^*_{\text{heter}} = \Delta G^*_{\text{homo}} f(m, R') \tag{7.15}$$

with

$$\Delta G^*_{\text{homo}} = \frac{16\pi\gamma_{\text{cf}}^3\Omega^2}{3[kT\ln(1+\sigma)]^2} \tag{7.16}$$

$$f(m,R') = \frac{1}{2} + \frac{1}{2}\left(\frac{1-mR'}{w}\right)^2 + \frac{1}{2}R'^3\left[2-3\left(\frac{R'-m}{w}\right)+\left(\frac{R'-m}{w}\right)^2\right] + \frac{3}{2}mR'^2\left(\frac{R'-m}{w}-1\right) \tag{7.17}$$

and

$$w = \left[1+\left(R'\right)^2 - -2R'm\right]^{1/2}. \tag{7.18}$$

Here $R'$ is actually the dimensionless radius of curvature of the substrate with reference to the radius of the critical nucleus $r_c$. Note that the factor $f(m,R')$ varies from 1 to 0. To acquire the details of (7.17,7.18), see Chap. 2 in this book or Refs. [54, 56]. Obviously, this factor plays an important role in the determination of the heterogeneous nucleation barrier $\Delta G^*_{\text{heter}}$. One can see from (7.9) that the influence of foreign particles on the nucleation barrier can be fully characterized by this factor.

Figure 7.3a shows that $f(m,R')$ is a function of $R'$ for a given $m$. When $R' \to 0$, $f(m,R') = 1$, implying that the foreign body "vanishes" completely as a nucleating substrate. In practice, if foreign bodies are too small, e.g., clusters of several molecules, nucleation on these substrates will not be stable. Then, they play no role in lowering the nucleation barrier. On the other hand, if $R' \gg 1$, the foreign body can be treated as a flat substrate with respect to the critical nuclei. In this case, $f(m,R') = f(m)$ is solely a function of $m$, and (7.17) is then reduced to

$$f(m,R') = f(m) = \frac{1}{4}(2-3m+m^3) \tag{7.19}$$

$f(m)$ as a function of $m$ is given in Fig. 7.3b.

### 7.3.2 Kinetics of Nucleation

The commonly accepted nucleation processes can be regarded as follows: on the substrate surface, some molecular processes occur due to transient visiting molecules that adsorb, form short-lived unions, break up, desorb, etc. An instantaneous census would show some distributions of subcritical nuclei (or clusters) with 1, 2, 3, ... molecules per cluster as,

$$\text{Monomer} \rightleftharpoons \text{Dimer} \rightleftharpoons (n--1)\text{mer} \rightleftharpoons n\text{–mer} \rightleftharpoons (n+1)\text{mer} \tag{7.20}$$

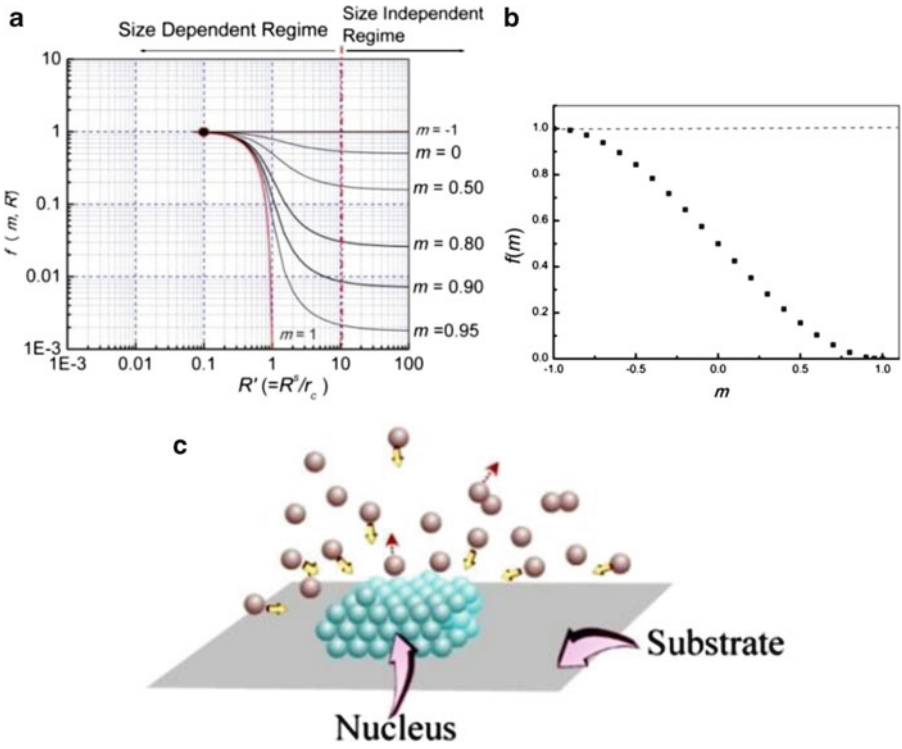


**Fig. 7.3** (**a**) Dependence of the interfacial correlation function $f(m,R')$ on $m$ and $R'$. (b) Measured $f(m,R')$ in ice nucleation [55–57]. (**b**) Dependence of the interfacial correlation function $f(m,R') = f(m)$ on $m$ at $R' \gg 10$. (**c**) Schematic illustration of *the shadow effect* of the substrate in heterogeneous nucleation. The presence of the substrate blocks the collision of growth units onto the surface of the nucleus. Reprinted with permission from Ref. [9] ©2004 Springer

Although many theories have been put forward, the "atomic" process has never been visualized and treated in a quantitative way until recently when a 2D nucleation process was monitored in the system of charged PS spheres driven by the alternating field with a fixed field strength and a frequency (i.e., Fig. 7.1) [13, 57]. A typical process of nucleation has been presented in Fig. 7.4. On the electrode surfaces, the concentration of particles was supersaturated and the particles started to form the nuclei (Fig. 7.4a, b, where we represented crystal-like particles as blue spheres). The nucleus in red circle kept growing whatever its state was pre- or post-nucleation; the nucleus in green circle shrank far more frequently than they grow (Fig. 7.4c–e). In Fig. 7.4f, the plots reflected the evolution of size of two adjacent nuclei during the process of pre-nucleation. One nucleus was growing larger and larger when its size is larger than the critical size. Moreover, the other nucleus was shrinking before reaching the critical size. This implies that nucleation is a number of simultaneous fluctuating assembly–disassembly events. A successful nucleation process corresponds to one of such events that can survive till the nucleus reaches critical size [53].

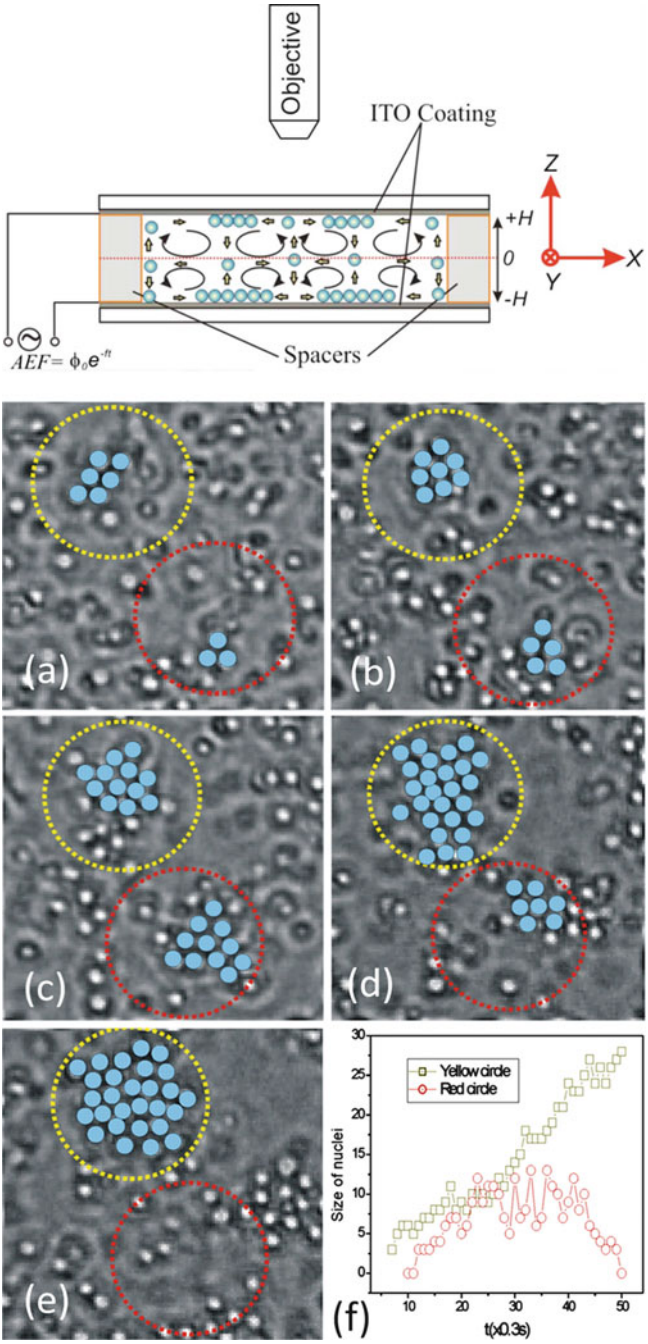


**Fig. 7.4** *The top schema*: the experimental setup. The colloidal suspension is sandwiched between two ITO-coated glass plates separated by insulating spacers. Snapshots of pre-nucleation process below: (**a**) Time $t = 10t_0$ ($t_0$ is the timing interval of images, 0.3 s), (**b**) $20\,t_0$, (**c**) $30\,t_0$, (**d**) $40\,t_0$, (**e**) $50\,t_0$, (**f**). The evolution of size of two nuclei. The *yellow curve* represents the increasing size of nucleus in the *yellow circle*; the *red curve* represents the shrinkage of nucleus in the *red circle*. ($\sigma_E = 2.6\times10^4$ V/m, $f = 600$ Hz) (From [13]). Reprinted with permission from Ref. [13] © 2004 Nature Publishing Group

In the case of the 2D nucleation of crystals with $n^*$ molecules, the homogeneous nucleation energy $[\Delta G^*_{\text{homo}}]_{2D}$ and the radius of critical size $(r_c)_{2D}$ are expressed by (7.21,7.22), respectively [13],

$$[\Delta G^*{}_{\text{homo}}]_{2D} = \frac{\pi \Omega (\gamma_{\text{step}})^2}{\Delta \mu} \tag{7.21}$$

$$[r_c]_{2D} = \frac{\Omega \gamma_{\text{step}}}{\Delta \mu} \tag{7.22}$$

where $\gamma_{\text{step}}$ is the crystal–liquid interfacial edge free energy.

The widely accepted kinetic model of nucleation (within the cluster approach) was used first by Farkas [3] in 1927. It is based on the Szilard scheme of successive "chain reaction" between monomer molecules and $n$-sized clusters as shown by (7.20).

A master equation for the concentration $Z_n(t)$ of the $n$-sized clusters at time $t$ is written in the form of a continuity equation [56, 58, 59]

$$\frac{dZ_n}{dt} = J_{n-1} - J_n, \tag{7.23}$$

where $J_n$ is the flux through point $n$ on the size axis. Thus in this formulation, $J$ is the flux through the nucleus size $n^*$, i.e., $J \sim J_{n*}(t)$, so that a time dependence is introduced in the nucleation rate.

The basic problem in the nucleation kinetics is to solve the master (7.20) in the unknown cluster size distribution $Zn(t)$, as knowledge on $Zn(t)$ will allow the acquirement of the nucleation rate. In this concern, three physically distinct states of the nucleating system require a special attention: *the equilibrium*, *the stationary* (*or steady*), and *the nonstationary states*. In the following, we will brief the equilibrium and the nonstationary states and focus more on the steady state, which is more relevant in the most nucleation events.

#### 7.3.2.1 Equilibrium State

As nucleation is a dynamic process other than that at equilibrium, this state is conceptual and never occurs in practices. Introducing this state is (1) to make a reference for other states and (2) to help in the treatment of the stationary state mathematically.

Based on the thermodynamic statistical principles, in equilibrium, $dZ_n/dt = 0$ and $J_n = 0$. Then $Z_n = C_n$ is the equilibrium cluster size distribution. ($C_n$ is the equilibrium concentration of $n$-sized clusters.) According to the Boltzmann law, one can easily obtain

$$(C_n/Z) = (C_1/\sum)^n \exp(-\Delta G_n/kT) \tag{7.24}$$

(for all $n$; $n = 2,3,4,\ldots$) with the effective total number of "molecules" per unit volume:

Let $\kappa_n$ be the rate of molecule addition. That is,

$$\kappa_n = \beta_{\text{kink}} K_n \tag{7.25}$$

where $K_n$ denotes the collision rate of monomers with an $n$-sized cluster and $\beta_{\text{kink}}$ is the conversion probability . Also let $\kappa'_n$ be the rate at which the cluster loses molecules. Obviously, at the equilibrium state, one has the detailed balance between the growth and disintegration of clusters,

$$\kappa_n C_n - \kappa'_{n+1} C_{n+1} = 0. \tag{7.26}$$

Since $\Delta G^*_{\text{heter}}(\Delta\mu)$ has a maximum at $n = n^*$, $C_n$ displays a minimum at the critical nucleus size. The increasing nonphysical branch of $C_n$ at $n > n^*$ reflects the fact that the mother phase is saturated.

#### 7.3.2.2 Stationary (or Steady) State

The stationary state is a state at which the cluster size distribution does not change with time. Normally, this state is so far the most important state and occurs in the middle stage of nucleation and can be treated quantitatively. In the stationary state, $dZ_n/dt = 0$. Because $J_n = \text{constant} = J_{n^*} = J$, $Z_n \sim Z'_n$ is the steady-state cluster size distribution. The stationary nucleation rate for homogeneous nucleation is given by the Becker–Doering formula [56]

$$J = \frac{zK^*}{v_m} \exp\left(-\frac{\Delta G^*_{\text{homo}}}{kT}\right) \tag{7.27}$$

with

$$z = \frac{Z'_{n^*}}{C_{n^*}} - \frac{Z'_{n^*+1}}{C_{n^*+1}} \tag{7.28}$$

where $z$ is the so-called Zeldovich factor [48, 59], $K^* = K_{n^*}$ is the frequency of monomer attachment to the critical nucleus, $v_m$ denotes the average volume of structural units in the ambient phase, and $C_n$ is the equilibrium concentration of $n$-sized clusters given by[49],

$$C_n \cong C_1 \exp(-\Delta G_n / kT) \tag{7.29}$$

Based on the definition of $J_n$, one has

$$J_n = k_n Z'_n \tag{7.30}$$

At the steady state, $J'$, that is the formation rate of critical nuclei per unit volume per unit time around a foreign particle is equal to the steady-state growth of clusters on the surface of the particle. The nucleation rate can then be given in terms of

$$J' = J_{n*} = J_n = \text{constant} = \text{criticalsizednucleiformed/unitvolume} - \text{time} \equiv \ldots$$
$$= k_n Z'_n - -k_{n+1} Z'_{n+1} = \text{constant}. \tag{7.31}$$

Regarding the effect of the substrate on both the nucleation barrier and the transport process, and the fact that the average nucleation rate in the fluid phase depends on the density and size of the foreign particles present in the system, the nucleation rate is given by [49, 56, 58]

$$J = 4\pi a (R^s)^2 N^{\circ} f''(m, R')[f(m, R')]^{1/2}$$
$$\times B \exp\left[-\frac{16\pi \gamma_{cf}^3 \Omega^2}{3kT[kT\ln(1+\sigma)]^2} f(m, R')\right] \tag{7.32}$$

with

$$B = (C_1)^2 4D\beta_{\text{kink}}\Omega\left(\frac{\gamma_{cf}}{kT}\right)^{1/2} \tag{7.33}$$

$$f''(m, R') = \frac{1 + (1 - R'm)/w}{2} \tag{7.34}$$

and

$$f''(m, R') = f''(m) = \frac{1}{2}(1 - m) \text{ at } R' >> 1 \tag{7.35}$$

where $B$ is the kinetic constant and $N^{\circ}$ denotes the number density of the substrates (or "seeds"). The growth of nuclei is subject to the effective collision and incorporation of growth units into the surfaces of the nuclei (cf. Fig. 7.3c). In the case of homogeneous nucleation, the growth units can be incorporated into the nuclei from all directions. However, for heterogeneous nucleation, the presence of the substrate will block the collision path of the growth units to the surfaces of these nuclei from the side of the substrate (cf. Fig. 7.3c). This is comparable to the "shadow" of the substrate cast on the surface of nuclei. $f''(m,R')$ in the pre-exponential factor, which is the ratio between the average effective collision in the presence of substrates and that of homogeneous nucleation (i.e., in the absence of a substrate), describes this effect.

Both $f(m,R')$ and $f''(m,R')$ are functions of $m$ and $R'$. When $R' \to 0$ or $m \to$ -1, $f(m,R')$, $f''(m,R') = 1$. This is equivalent to the case of homogeneous nucleation. In the case where $m \to 1$ and $R \gg 1$, one has $f(m,R')$, $f''(m,R') = 0$. Normally,

heterogeneous nucleation occurs in the range between 1 and -1, or $f(m,R')$ between 0 and 1, depending on the nature of the substrate surface and the supersaturation.

Note that for homogeneous nucleation, one has $f\prime\prime(m,R') = f(m,R') = 1$ and $4\pi a(R^s)^2 N^o \to 1$. In this case, (7.32) is converted to

$$J = B \exp\left[-\frac{16\pi\gamma_{cf}^3\Omega^2}{3kT[kT\ln(1+\sigma)]^2}\right]. \tag{7.36}$$

This implies that (7.29) is applicable to both homogeneous and heterogeneous nucleation.

Similar to 3D nucleation, 2D nucleation can also adopt a similar form [49]:

$$J_{2D} = \left\{\frac{2D_s C_1^2}{\pi}\left[\frac{\Omega\ln(1+\sigma)}{h}\right]^{1/2} \exp\left(-\frac{\Omega(\gamma_{cf}^{\text{step}})^2\pi h}{(kT)^2\ln(1+\sigma)} f_{2D}(m_{2D}, R'_{2D})\right)\right\}$$
$$\times \beta_{kink}\delta\left(m_{2D}, R'_{2D}, R^s, N^o\right) \tag{7.37}$$

with

$$\delta(m_{2D}, R'_{2D}, R^s, N^o) = \left\{\frac{\psi}{\pi} N^o \pi a R'_{2D}\left[f_{2D}(m_{2D}, R'_{2D},)\right]^{1/2}\right\} \tag{7.38}$$

where $D_s$ denotes the surface diffusivity. In the case of 2D homogeneous nucleation, one has $\delta(m_{2D}, R'_{2D}, R^s, N^o) = f_{2D}(m_{2D}, R'_{2D})$, and (7.37) can be simplified as follows:

$$J_{2D} = \left\{\frac{2D_s n_1^2}{\pi}\left[\frac{\Omega\ln(1+\sigma)}{h}\right]^{1/2} \exp\left(-\frac{\pi\Omega h\gamma^2}{(kT)^2\ln(1+\sigma)}\right)\right\} \beta'_{\text{kink}} \tag{7.39}$$

Here $n_1$ is the number of single particles (monomers), and $\beta_{\text{kink}}$ is the sticking possibility.

#### 7.3.2.3 Nonstationary (or Nonsteady) State

From the initiation of nucleation ($t = 0$) to the stationary/steady state, there must be a transit state where the size distribution of clusters will change with time. This state is known as the nonstationary (or nonsteady) state. Similarly, when nucleation comes to the end, we will also experience this state. When the nucleation is nonstationary, $dZ_n/dt \neq 0$, and flux $J_n$ is a function of both $n$ and $t$. The nucleation rate is then time dependent and this nonstationary nucleation rate $J_{\text{nonst}}(t) = J_{n^*}(t)$. In other word, $J_{\text{nonst}}(t)$ will change with time.

#### 7.3.2.4 Experimental Verification of Nucleation Kinetics Based on Colloidal Crystallization

Although theoretical analysis on the above states of nucleation has been published for long time, experimental verification, in particular, the direct measurement for the distribution of subcritical nuclei had never been achieved till recently when the electrically controlled 2D colloidal nucleation was carried out [13]. By measuring the size distribution of subcritical nuclei on the surface of flat electrode, we observed the evolution among the different kinetics: nonstationary, stationary, and equilibrium states [49] in the process of pre-nucleation. Figure 7.5a presented a typical distribution at different time. Once the driving force is applied, the small nuclei are formed. Subsequently, the cluster size exceeded the critical size of nuclei, and the nuclei were growing to the crystallites gradually. Figure 7.5a reflected this image of nucleation kinetics. Here we defined a transient point $n^*(t)$, where the size distribution approached to a steady number of clusters in the nucleation (see Fig. 7.5a, inset).

It follows from Fig. 7.5 that, first, the system starts from a nonstationary state ($t = 3.2$ s) at the beginning and gradually approaches toward the stationary state ($t > 20$ s) in which the distribution of nucleating clusters $Z_n$ is independent of time. Second, a nucleation event is successful once the distribution of nucleating clusters $Z_{n^*} = 1$ in any time. Therefore, the cluster size at $Z_n = 1$ can be defined as the critical size of nucleation $n^*$.

Before reaching the stationary state, $n^*$ is time dependent. Only after reaching the stationary state, the critical size of nucleus $n^*$ can acquire a constant value (Fig. 7.5b). In other words, it makes sense to discuss the critical size of nucleus only at the stationary state.

In Fig. 7.5c, the average nucleation rate in the unit area of surface according to the fitting slope of curves was measured. Figure 7.5d presents the nucleation rate density under different driving forces. The linear fitting of the plot of $\ln(J)$ $1/\ln(1+\sigma)$ indicates that (7.39) can be applied to quantify the nucleation kinetics of 2D nucleation.

### *7.3.3 Initial Stage of Nucleation: Is Classical Nucleation Theory Accurate?*

Although the basic treatments of classical nucleation theories (CNTs) have been approved to be correct as shown in Sect. 7.3.2.3, some aspects of nucleation remain unclear. In the analysis of nucleation kinetics in Sect. 7.3.2, the structure of crystal nuclei is supposed to be identical to the bulk crystals. Is this assumption correct? If not, what are the consequences? In the following, we will describe the interfacial structural evolution during nucleation, the impact of the interfacial structure of nucleating clusters on the nucleation energy barrier, in terms of 2D colloidal crystallization model system.

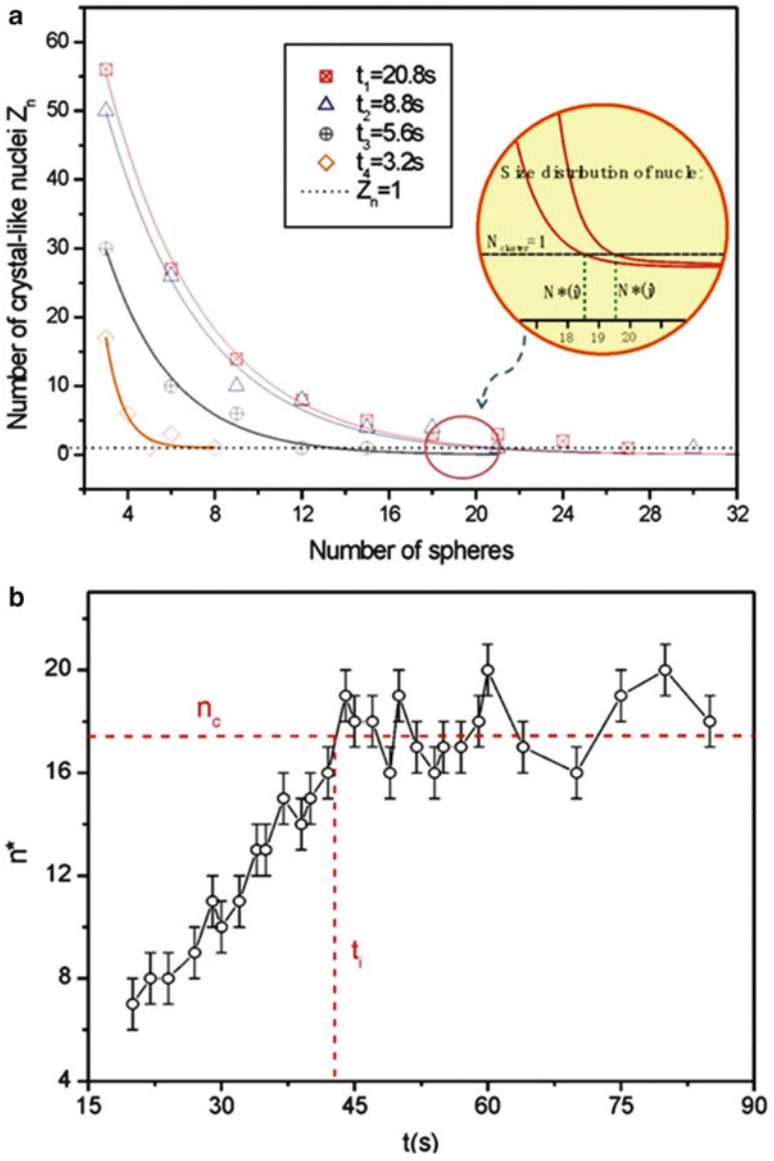


**Fig. 7.5** Measurement of nucleation kinetics parameters. (**a**) The typical size distribution of subcritical nuclei versus time ($\sigma_E = 2.6\times10^4$ V/m, $f = 600$ Hz.). (**b**) $n^*(t)$ versus time. After the induction time, $n^*(t)$ becomes stable. The critical size can be determined. (**c**) The number of nuclei for which the size is larger than the critical size in different time. We can measure the nucleation rate in the unit area according to the slope of linear fitting of this *curve*. (**d**) The nucleation rate under the different supersaturation (driving force). The *straight line* fitting is based on (7.39). From (7.39), we also can get the line tension of interface. The value of $\gamma_{step}$ is $0.50kT/a$ ($a$ is the diameter of colloidal particles), which is in agreement with the measurements. For more details, see Ref. [15]. Reprinted with permission from Ref. [13] © 2004 Nature Publishing Group

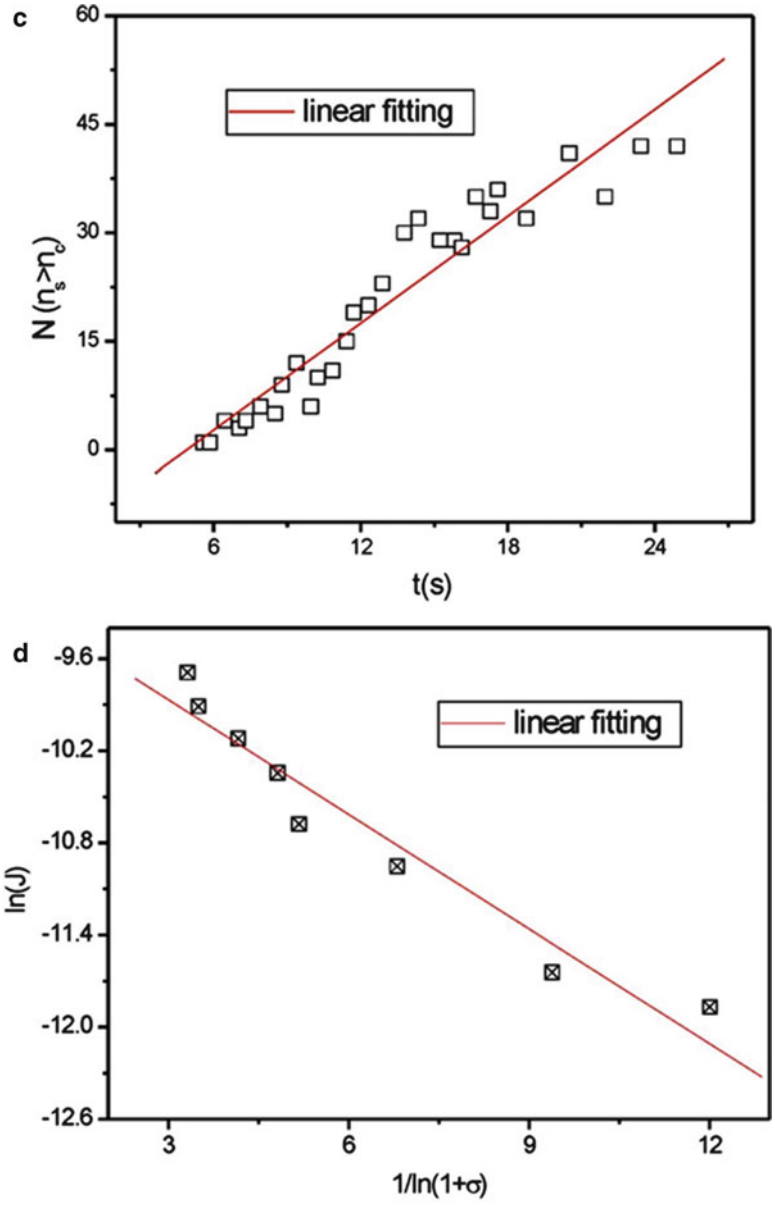


**Fig. 7.5** (continued)

To identify the crystalline-like particles from the liquid-like particles in 2D crystal nuclei, a local 2D bond-order parameter is defined as follows [37–41]:

$$\psi_6(r_i) = M^{-1}\left|\sum\nolimits_j e^{i6\theta_{ij}}\right| \tag{7.40}$$

where $r_i$ is the center of particle $i$, and $\theta_{ij}$ is the angle subtended between the vector from particle $i$ to its $j$th nearest neighbor and the arbitrarily chosen $x$ axis. $M$ is the number of nearest neighbors of particle $i$. The mean value of $\psi_6(r_i)$ for crystalline structures obtained from the experiments is 0.8, which is taken as the criterion for a crystal-like particle.

Figure 7.6a reveals that at relatively low supersaturations, the structure of crystalline clusters is a bit fluid-like and more disordered at the beginning and gradually approaches to the ordered structure in the bulk crystalline phase at a size close to the critical size of nuclei. The transition from the initial metastable structure to the final stable structure is a continuous process.

On the other hand, at high supersaturations (decreasing frequency gives rise to the increase in supersaturation) [60], Fig. 7.6b shows the structural transition occurring under conditions of $f = 3{,}000$ Hz and $V_{pp} = 2.5$ V. Different from the behavior of $\langle\psi_6\rangle$ in Fig. 7.6(a), $\langle\psi_6\rangle$ can be as high as 0.8 instantaneously even before it reaches its transition size ( 30) (in Fig. 7.6b(i)). This implies that the nucleus can have a crystalline structure even before it becomes stable in structure. Nevertheless, the crystalline structure of the precritical nuclei is transient and fluctuated. In Fig. 7.6b(ii) and (iv), the structure of the nucleus is ordered. In the subsequent seconds, as shown in Fig. 7.6b(iii) and (v), it becomes disordered again. Only when the size is beyond the critical size 30, the crystalline structure becomes stable. As the supersaturation is increased further by decreasing frequency, $\langle\psi_6\rangle$ remains more or less 0.8 in the whole growth process from the beginning, and crystal nuclei are initially created with a crystalline structure as suggested by CNT [44].

The results in Fig. 7.6 indicate that the initial structure of crystal nuclei and the structural evolution of crystal nuclei are *supersaturation-dependent*. At low supersaturations, a metastable liquid-like structure is likely to occur first. This is

**Fig. 7.6** (continued) a critical size. (*iv*) $\langle\psi_6\rangle$ is a function of nuclei size $N$. Monodisperse colloidal particles (polystyrene spheres of diameter 0.99 mm, polydispersity <5%, Bangs Laboratories) were dispersed uniformly in deionized water. The colloidal suspension was then sealed between two parallel horizontal conducting glass plates coated with indium tin oxide (*ITO*).The gap between the two glass plates is $H = 120 \pm 5$ mm. The dynamic process is recorded by a digital camera (*CCD*) for analysis. *AEF* alternating electric field. (**b**) Phase diagram of the system when the concentration of $Na_2SO_4$ is $2 \times 10^{-4}$ M. $V_{pp}$, peak-to-peak voltage. Due to the nature of 2D crystals, $\langle\psi_6\rangle$ for a perfect 2D crystal is 0.8. (**b**) Transient crystalline structure of nuclei under condition of $V_{pp} = 2.5$ V, $f = 3{,}000$ Hz. (*i*) Fluctuation of order parameter during the growth. (*ii*, *iii*) Due to the structural fluctuation, nuclei can have a transient crystalline structure. (*iv*, *v*) Liquid-like structure displayed by precritical nuclei. Reprinted with permission from Ref. [44] © 2008 Wiley-VCH Verlag GmbH & Co

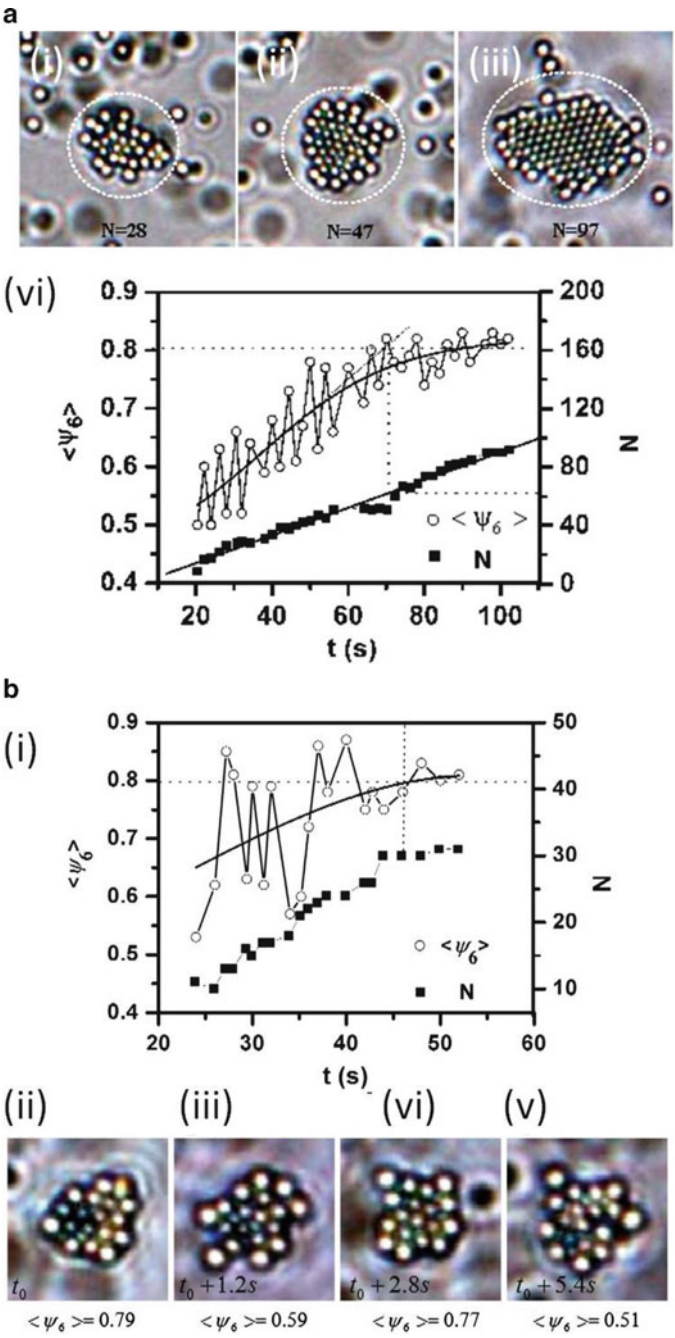


**Fig. 7.6** (**a**) Structural evolution of nuclei under conditions of $V_{pp} = 2.5$ V, $f = 5{,}000$ Hz. (*i*) Initial structure of nuclei is liquid-like. (*ii*) As the nucleus grows, its core first becomes ordered with the exterior layer remaining liquid-like. (*iii*) The nuclei become completely ordered after they exceed

because the nucleation barrier is very high at low supersaturations (cf. (7.16) and (7.21)). The occurrence of the metastable structure at the nuclei may help to reduce the nucleation barrier [61, 62]; therefore, it is kinetically more favorable. On the other hand, the nucleation barrier becomes much lower at higher supersaturations (cf. (7.16) and (7.21)), and the structural relaxation of nuclei is not kinetically very favorable. Therefore, the structure of pre-nucleation clusters can be as ordered as that of the bulk crystalline phase.

The analyses on the kinetic data [34, 36, 44] confirm that, at low supersaturations, the evolution of nuclei from a liquid-like structure to a crystal-like structure will effectively reduce nucleation barrier and facilitate the nucleation dynamics. In other words, at low supersaturations, the CNTs overestimate the nucleation barrier. At high supersaturations, as the nucleation barrier decreases substantially. Adopting the structure of the bulk crystals during nucleation need not be energetically unfavorable. Therefore, the dynamic behavior predicted by the CNTs becomes valid.

### *7.3.4 Multistep Nucleation/Crystallization in Biomineralization*

In the case of biomineralization, it is often found that the most thermodynamically stable calcium phosphate phase, hydroxyapatite ($Ca_{10}(PO_4)_6(OH)_2$ or $Ca_5(PO_4)_3(OH)$, HAP), does not occur first. Instead, the least stable phase, the amorphous calcium phosphate (ACP) phase, occurs at the beginning and then transforms into more thermodynamically stable phases in solutions. Pan and Liu [63] applied the combined in situ UV–vis extinction detection and ex situ electronic microscopy to examine the formation of ACP and the evolution to HAP under the physiological pH and ionic strength condition in a simulated body fluid. The UV–vis extinction spectroscopy was applied to monitor the mineralization process (Fig. 7.7).

According to the UV–vis extinction curves, the mineralization process can be divided into four stages (Fig. 7.7b). In stage I, after the mixing of a calcium solution and a phosphate solution, ACP occurs, and the solution becomes turbid. In stage II, the extinction of the solution arises and gradually reaches a plateau. In this stage, the aggregation of ACP occurred (Fig. 7.8a). In stage III, an abrupt decrease in the extinction is observed, corresponding to the transformation of ACP mineral to HAP crystallites (Fig. 7.8b, e–g) [64, 65].

Afterward, the crystallites undergo further growth, ripening and aggregation in stage IV. The final products are some spherulites, composed of platelet crystallites organized in the radial orientation (Fig. 7.8c,i). The characteristic four stages in the UV–vis extinction curves can be found from the solutions of different calcium and phosphate concentrations [63]. The details of the morphological change and phase evolution of ACP were captured by ex situ EM. The spherical-liked minerals ($215 \pm 29$ nm) were first formed (within 3 min, Fig. 7.8a,d). The selected area

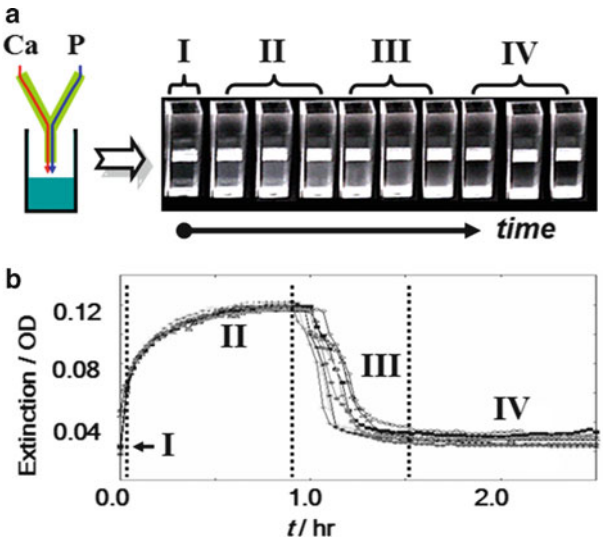


**Fig. 7.7** The evolution of calcium phosphate solution. After the mixing of a calcium solution with a phosphate solution (with final concentration: 4 mM $CaCl_2$, 6 mM $K_2HPO_4$, 150 mM NaCl, pH 7.40, i.e., the saturation indices (log (*IAP*) - log ($K_{sp}$), where *IAP* is the ionic activity product of precipitation; $K_{sp}$ is the solubility product constant) of initial solution were 0.25 (for ACP, $Ca_9(PO_4)_6$), 25.8 (for HAP), 23.1 (after the precipitation of ACP), the solution became turbid gradually. In about 1 h, the suspension suddenly became clear, accompanied with visible sedimentations formed simultaneously (see (**a**)). The entire mineralization process can be monitored by the extinction curves (the optical difference of 405 nm and 550 nm). (**a**) Photographs of the suspensions. The solution became turbid, then clear again accompanied with the sediment of minerals. (**b**) The extinction curves of calcium phosphate solutions. Reproduced with permission from Ref. [63] © The Royal Society of Chemistry 2010

election diffraction (SAED) patterns of diffusive rings indicate that the spheres are amorphous (Fig. 7.8a). The initially round-shaped ACP particles indicate the occurrence of fluid-like structure at the beginning. The sintering of the submicro-sized ACP droplets in solutions leads to the further aggregation of these spheres (Fig. 7.8a). The ACP aggregate partially merged as showed in Fig. 7.8d. After the formation of ACP, the particles remained in amorphous state for about 1 h before the transformation took place.

Concerning the transformation of ACP spheres, at first, the boundary of ACP spheres became polygonal-like (Figs. 7.8b,e and 7.9a; 67 min). Some condensed rings or dots appear in the SAED patterns (Fig. 7.8b), indicating the formation of crystalline materials. The bright dots in the dark-field TEM images (DF-TEM) (Fig. 7.9b) indicate the occurrence of crystallized minerals. The high-resolution TEM images (HR-TEM) (Fig. 7.9c) directly show that the crystallization happens at the surface of the ACP spheres, while the main portion of the sphere remains amorphous (i.e., fast Furrier transform (FFT) patterns of selected region in Fig. 7.9c, region 3).

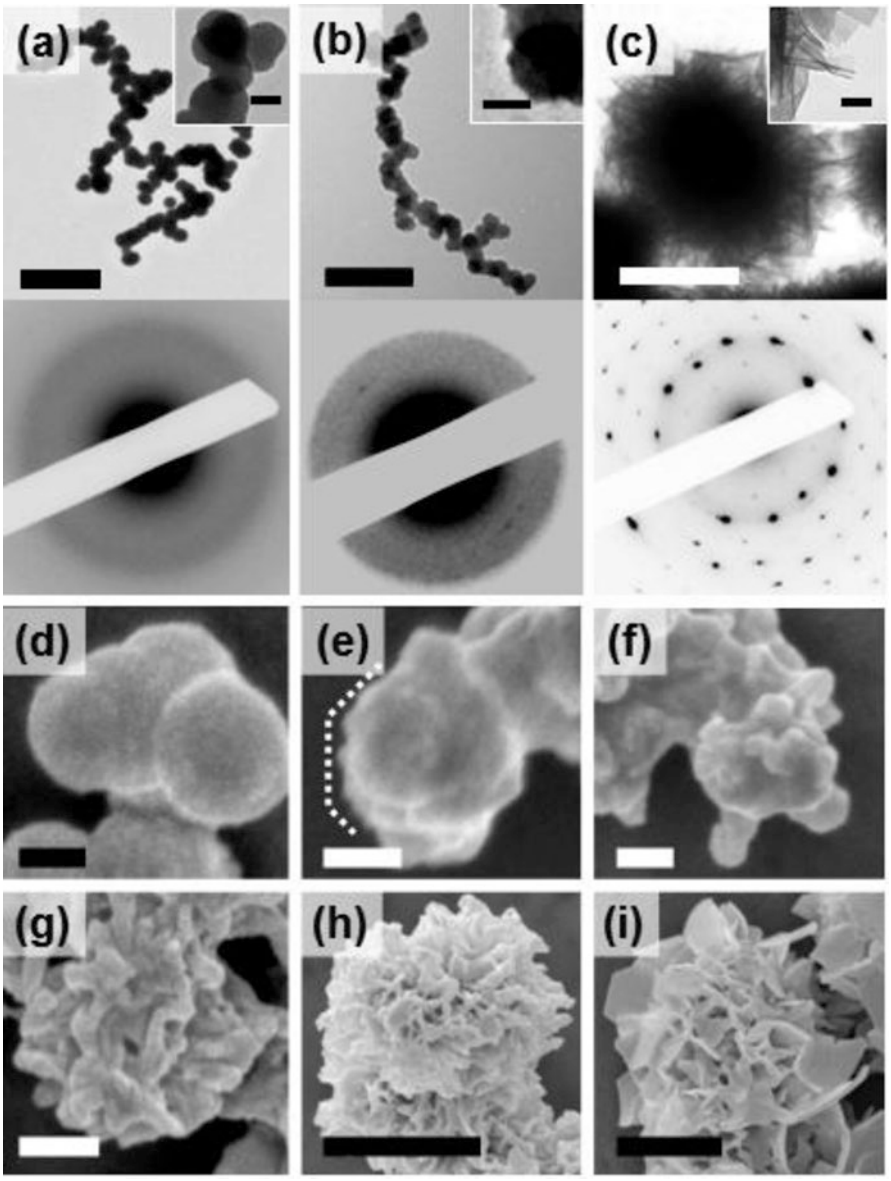


**Fig. 7.8** Phase and morphology evolution of calcium phosphate minerals. (**a**–**c**) TEM images and SAED patterns of the precipitates. (**a**) Initially formed ACP spheres. Bar: 1 μm and 100 nm (subimage). (**b**) Intermediate state of ACP. Bar: 1 μm and 100 nm (subimage). (**c**) Final spherulite HAP. Bar: 1 μm and 200 nm (subimage). (**d**–**i**) SEM images of the evolution of ACP. (**d**) 3 min. (**e**–**g**) 67–73 min. (**h**) 90 min. (*i*) 7 h. Bar: (**d**–**f**) 100 nm; (**g**) 200 nm; (**h**–**i**) 1 μm. The selected area diffraction (*SAED*) study together with XRD examination indicates that the mineral phase is HAP, and each platelet in a spherulite arm is a single crystallite (see (**c**)). Reproduced with permission from Ref. [63] © The Royal Society of Chemistry 2010

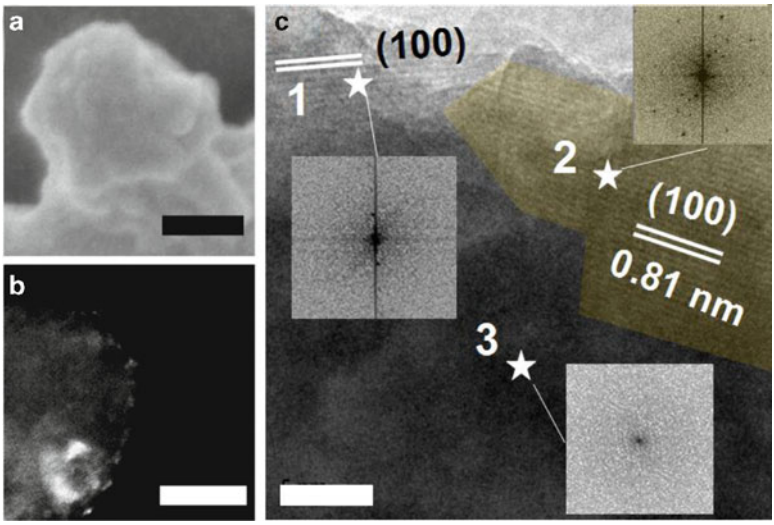


**Fig. 7.9** Initial phase transformation stage of ACP particles. (**a**) SEM image (**b**) DF-TEM image. (**c**) HR-TEM image, and the fast Fourier transform (*FFT*) patterns of crystallized regions (*1*, *2*) and the amorphous region (*3*). Bar: (**a**) 100 nm; (**b**) 50 nm; (**c**) 10 nm. Reproduced with permission from Ref. [63] © The Royal Society of Chemistry 2010

The above results indicate that at the initial stage of biomineralization in a simulated body fluid solution, ACP spheres occur soon after mixing the two reactants. The transformation from ACP to HAP takes place in about 1 h. During the transformation, the nucleation occurs preferably at the surface of ACP spheres. The embedded/adhered crystallites on the ACP surface would not allow the crystallites to rotate their orientations and/or relocate from their relative positions. This gives rise to the formation of the HAP spherulites.

The process outlined above is a typical stepwise crystallization, the so-called two-step crystallization (TSC) [66]. It is one way to facilitate the nucleation kinetics and often observed during protein crystallization [10, 67–69], biomineralization, etc. According to TSC, dense amorphous droplets are first formed from the mother phase; crystalline nuclei are then created from the droplets. For instance, during the formation of calcite in sea urchin larvae, a transient amorphous phase is formed first, before the final crystal phase is reached [70, 71]. Similarly, a transient amorphous phase is also identified during the formation of aragonite controlled by mollusk bivalve larvae [72]. Recently, the similar process has also been observed for the HAP formation from a simulated body fluid [73]. It is widely believed that in biological systems, the development of crystalline structures characterized by well-defined shape and size is essentially facilitated by the occurrence of transient amorphous phases [64, 71, 72]. In fact, recent studies indicated that TSC may be a mechanism underlying most crystallization occurring in typical atomic systems [62, 73, 74].

Although the TSC can be captured by Ostwald's rule· [17], the detailed understanding has not been acquired till recently. In this regard, the controlled colloidal assembly can be applied to examine the mechanism. MSC has attracted much attention in the past decade due to its importance in both scientific and technological points of view. However, the understanding of TSC remains to be insufficient. A key challenge is that the kinetics creating the initial crystalline nuclei from the dense droplets is unclear and thus it is no way to predict the overall nucleation rate $J_c$ of crystals. In the following, we will recap the multistep crystallization (MSC) in the colloidal model system. The kinetics of MSC is discussed and a mathematical method is developed to address the local nucleation rate $j_c$ of crystal in the droplets.

A typical process of MSC, observed under conditions of $V_{pp} = 2.0$ V and $f = 800$ Hz, is presented in Fig. 7.10. Colloidal particles in the initial mother solution are uniformly distributed in the solution (i.e., Fig. 7.10a).

When an AEF is applied to the system, colloidal particles are transported onto the glass surface where they first form dense droplets (Fig. 7.10b). Subsequently, a few subcrystal nuclei are created from the droplets as illustrated in Fig. 7.10c. These subnuclei are not stable and will dissolve soon after they are created. Experimentally, it is found that the crystalline nuclei in the droplets have to acquire a critical size $N^*_{cry}$ before they can grow stably in the droplets as shown in Fig. 7.7d. In the experiments, every droplet can produce only one stable crystal. Moreover, to form a stable crystal beyond $N^*_{cry}$, the droplets have to first acquire a critical size $N^*$. It is found that although, at an early stage, many small dense droplets are created, only 3 or 4 out of 20 droplets can reach the critical size $N^*$ and develop successfully into a stable crystal. This is consistent with previous observations in protein crystallization [75, 76]. However, it is contradicting with the assumption by Kashchiev et al. [77]. A detailed analysis on the overall nucleation rate $J_c$ of MSC, determined by the local rate $j_c$ in the individual dense droplets, is given in Ref. [52].

In general, the MSC in a colloidal model system indicates that amorphous dense droplets first nucleate from the mother phase. Subsequently, a few unstable subcrystalline nuclei can be created simultaneously by fluctuation from the tiny dense droplets, which is different from previous theoretical predictions. Notice that it is necessary for these crystalline nuclei to reach a critical size $N_{cry}$ to become stable. However, in contrast to subcrystalline nuclei, a stable mature crystalline nucleus is not created by fluctuation but by coalescence of subcrystalline nuclei, which is unexpected. To accommodate a mature crystalline nucleus larger than the critical size $N_{cry}$, the dense droplets have to first acquire a critical size $N^*$. This implies that only a fraction of amorphous dense droplets can serve as a precursor of crystal nucleation. As an outcome, the overall nucleation rate of the crystalline phase is, to a large extent, determined by the nucleation rate of crystals in the dense droplets, which is much lower than the previous theoretical expectation. The calculations indicate that the MSC is indeed kinetically more favorable than one-step crystallization under the given conditions [41].

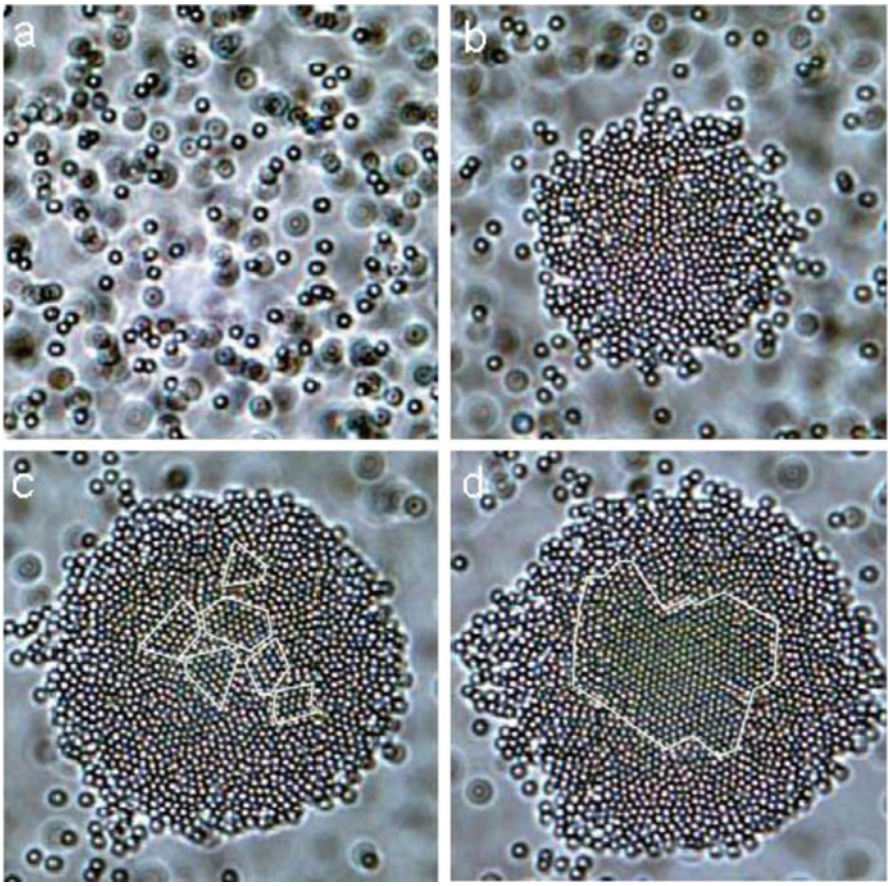


**Fig. 7.10** Multistep crystallization: (**a**) Initial dilute liquid phase. (**b**) Amorphous dense droplets are first created from the mother phase. (**c**) A few subcrystal nuclei are created from the amorphous phase. (**d**) A stable crystal is formed from the dense droplets. Colloidal suspension is sealed between two pieces of ITO-coated conducting glass plates separated by insulating spacers. The gap between the two glass plates is $H = 120 \pm 5$ μm. The dynamic process is recorded by a digital camera for analysis. (**b**) Phase diagram of the colloidal suspension. Monodisperse colloidal particles (polystyrene spheres of diameter 0.99 μm, polydispersity < 5%, Bangs Laboratories) are dispersed uniformly in deionized water. In the case, the volume fraction 0.03% of colloidal solid is chosen, and the surface potential of the colloidal spheres is adjusted to -72 mV by $Na_2SO_4$ ($10^{-4}$ M). The pH of the suspension is measured at 6.35. Monodisperse colloidal particles are dispersed uniformly in deionized water. Reproduced with permission from Ref. [40] ©2003 American Chemical Society

### 7.3.5 *Formation of Ordered and Disordered Structures in Biominerals*

Many living organisms rely on hard tissues, which are composed of biominerals and protein matrices with exquisite microarchitectures, for support, protection, and defense [78–80]. Natural composite materials such as teeth, bones, and shells represent intriguing and diverse design paradigms for exploring the relationships between structure and mechanical properties such as fracture toughness, stiffness, and hardness[81]. Despite the variety of these complex hierarchical architectures, biominerals are generally organized in a certain order to harden or stiffen tissues in living organisms. Although it is quite clear that the composite character of these materials plays an important role, some important questions need to be addressed. For example, how can the self-assembled nanocomposites exhibit superior mechanical characteristics? What are the key structural factors leading to the superior strength of hard tissues? Although the mechanical properties of hard tissues can be affected by the factors, cf. the type of minerals, the degree of mineralization, and size of mineral particles, there is still a striking variation in mechanical properties even when the components of the composites are similar [82, 83]. Combined with nanoindentation, Jiang and Liu [83] applied the position-resolved small-angle X-ray scattering and electron microscopy to examine the correlation between the microstructure of the enamels of human teeth and the mechanical properties.

The human tooth enamels can be roughly regarded as a bundle of nano HAP crystallite needles ( 94%) that sandwiched some proteins and water. It follows the experiments [83] that the degree of ordering of the biominerals varies strikingly within the dental sample, showing that both the hardness $H$ and the elastic modulus $E$ increase predominantly with the ordering of the biomineral crystallites [83] (see Fig. 7.11).

The mechanism concerning the toughness enhancement of hard tissues *vs* the improvement of the crystallite alignment are not entirely clear. Nevertheless, the following so-called crack stopper model may provide some physical insight into this matter. As indicated in Fig. 7.12, normally, crystals are never perfect. Instead, many defect lines or more seriously many grain boundaries may occur in crystals. The letter can even form the mosaic structure, composed of micro-crystallite grains that are misfit to a small degree with respect to each other (Fig. 7.12a). At collision, the crack may occur at the surface and easily propagate across the crystals along the defect lines or the grain boundaries (Fig. 7.12a). This results in the breakage of the crystals. On the other hand, for a block of crystallite assembly in which lamella or needle-like nano crystallites are packed in parallel to the surface (see Fig. 7.12b), a serious collision will also cause a crack at the surface of the block. Nevertheless, the propagation of the crack along the defect lines, or the grain boundaries at the surface, will be stopped at the interface between the parallel packed crystallites, preventing the crack propagating across the block (see Fig. 7.12b). In other words, this parallel packing structure in a crystallite assembly will prevent the breakage versus the penetration of the crack lines across the crystallite assemblies.

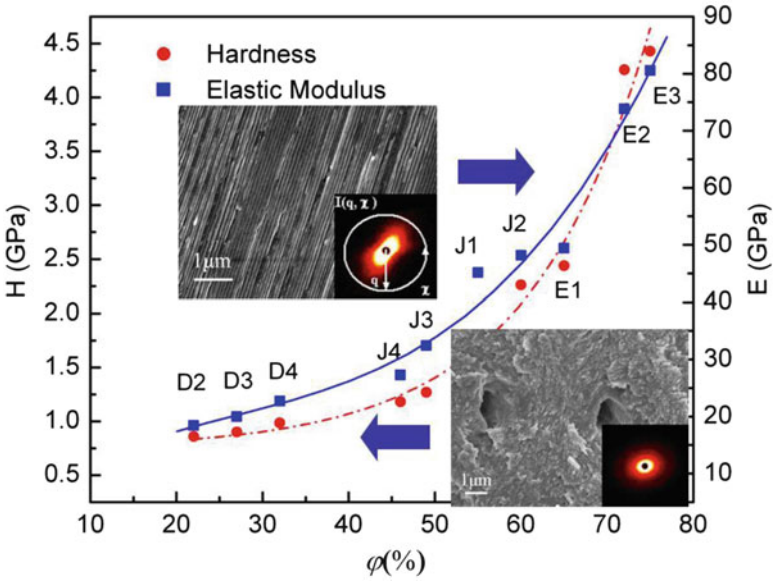


**Fig. 7.11** Quantitative correlation between mechanical properties and local alignment of minerals within the dental sample. Hardness versus alignment. Elastic modulus versus alignment. The *solid circles* and the *hollow circles* represent data measured from dental enamel and dentin, respectively. φ is an ordering parameter measured by small angle X-ray scattering. For a completely aligned assembly of crystallites, $\varphi = 100\%$, while for a completely disordered assembly, $\varphi = 0$. Reproduced with permission from Ref. [83] ©2005 American Institute of Physics

Now, the key question to be addressed is how this parallel packing structure in the bundle of crystallites occurs. One of the well-accepted interpretation is *the self-epitaxial nucleation-induced assembly* and the *supersaturation-driven interfacial structural mismatch* [9, 76, 84–86].

A typical example of *the self-epitaxial nucleation-induced assembly* and the *supersaturation-driven interfacial structural mismatch* is illustrated in Fig. 7.13a. As shown, in a solution growth, calcite crystals evolve from single crystals to polycrystals with supersaturation. At relatively low supersaturations, the polycrystals are well aligned with each other. The polycrystallites altogether form a well-aligned crystallites assembly. This is the so-called *self-epitaxial nucleation-induced assembly*. As with further increase in supersaturation, the structural match between the adjacent crystallites in the assembly is lost, giving rise to the *supersaturation-driven interfacial structural mismatch* (Fig. 7.13a).

Before going into the details of the model, let us first review the relevant nucleation processes. Kinetically, the occurrence of substrates in heterogeneous nucleation will on one hand lower the nucleation barrier thus leading to an increase in the nucleation rate, but on the other hand it will exert a negative impact on the surface integration. Nucleation on a substrate will reduce the effective collision of structural units to the surface of clusters (cf. Fig. 7.3c), where the structural

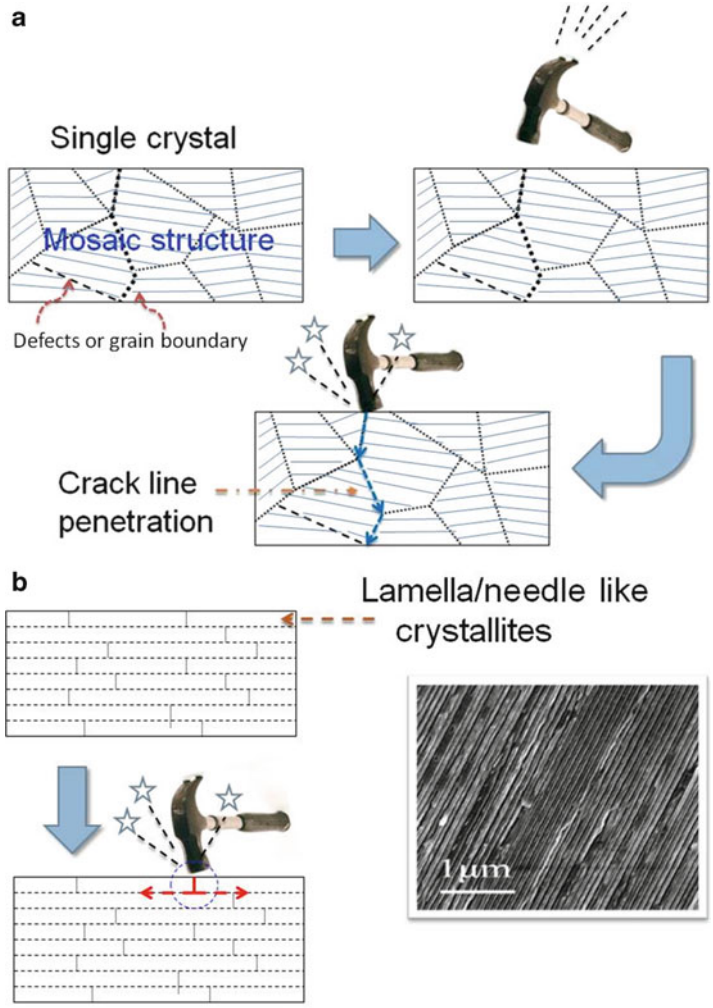


**Fig. 7.12** The crack stopper. Parallel packing of lamella or needle-like crystals will stop the crack line to penetrate the bundled crystallites. (**a**) The mosaic structure of a crystal causes the propagation of crack line, leading to the breakage of the crystal. (**b**) The parallel packing of lamella or needle-like crystallites in a crystallites assembly will stop the propagation of the crack line from one crystallite to the adjacent crystallites

units are incorporated into the crystal phase. This will slow down the nucleation kinetics, whose effect is contrary to the effect of lowering the nucleation barrier. As mentioned above, the latter effect, the so-called *shadow effect* of the substrate, is reflected in the appearance of $f''(m)$ and $f(m)$ in the pre exponential term of (7.32).

These two controversial effects play different roles in different regimes. At low supersaturations, the nucleation barrier is very high (cf. (7.33) and (7.34)). The

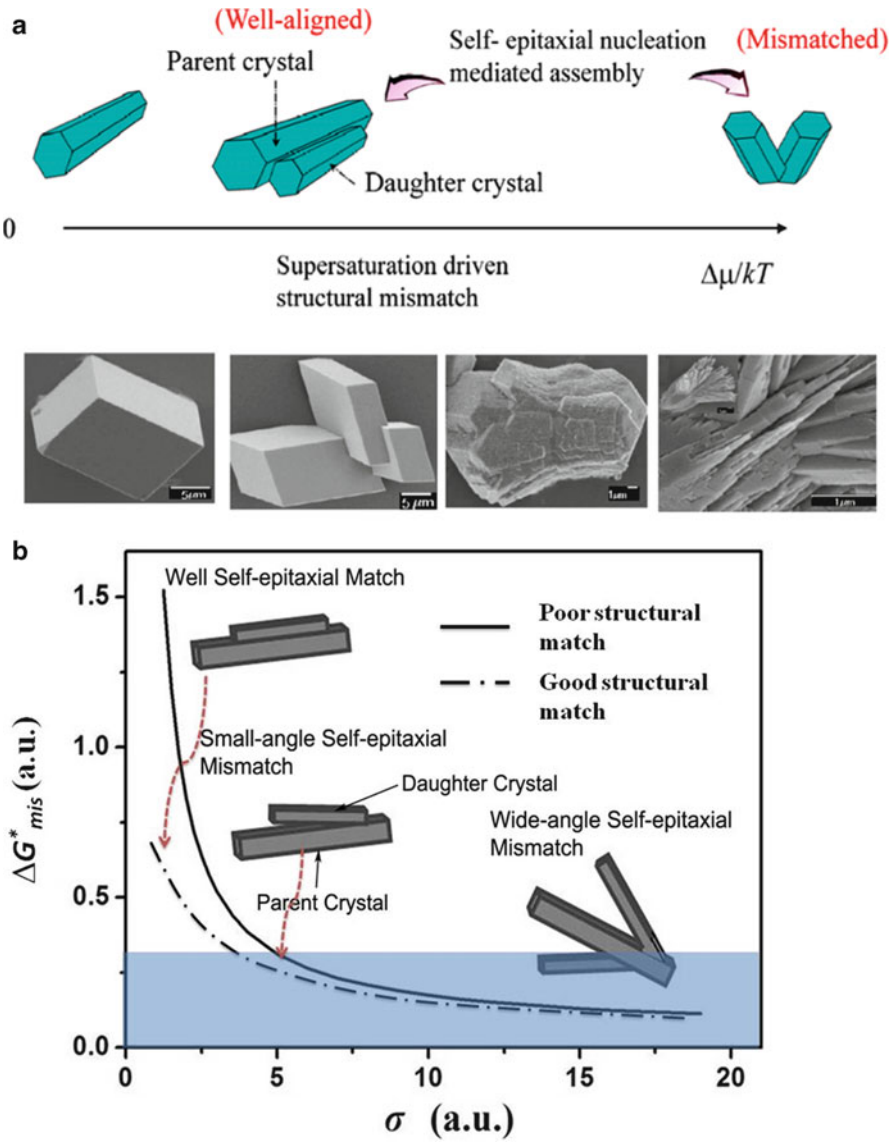


**Fig. 7.13** (**a**) Self-epitaxial nucleation induced assembly and supersaturation-driven interfacial structure mismatch nucleation: the structural match between the daughter crystals and the parent crystal will become poor as supersaturation increases. An example in calcite crystallization is demonstrated. (**b**) The change of the mismatch nucleation barrier $\Delta G^*_{\text{mis}}$ with supersaturation (cf. (7.16)). (**c**) The plot of $\ln t_s$ versus $1/[\ln(1+\sigma)]^2$ for $CaCO_3$ (calcite) nucleation. Within the range of supersaturations where experiments were carried out, three straight lines with different slopes intercept one another, dividing the space into three regimes. (**d**) Supersaturation-driven interfacial structural mismatch: with the increase in the supersaturation, the interfacial correlation factor $f(m)$ will increase abruptly at a certain supersaturation, such as A, B, . . . , corresponding to the transition from an ordered and structurally matched to a less ordered and structurally mismatched

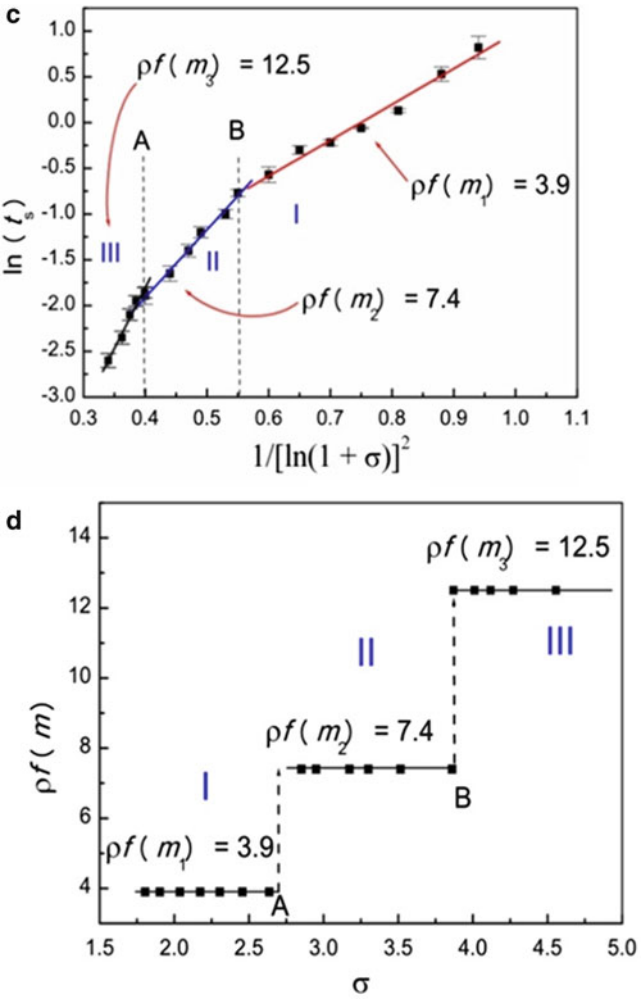


**Fig. 7.13** (continued) biomineral/substrate interface. (**a**) Reprinted with permission from Ref. [30] © 2008 Wiley-VCH Verlag GmbH & Co. (**c**, **d**) Reproduced with permission from Ref. [84] ©2003 American Chemical Society

nucleation rate will be substantially enhanced if the nucleation barrier is suppressed effectively ($f(m) \to 0$). Therefore, heterogeneous nucleation with a strong interaction and optimal structural match between the substrate and the nucleating phase will be kinetically favored. In this case, the nucleation of crystalline materials will be best templated by substrates capable of providing the excellent structural correlation with the crystalline phase. The structural synergy between the nucleating phase and the substrate will be optimal under this condition [84, 87].

The observation in Fig.7.13a can be understood as follows: the occurrence of daughter crystals on the parent crystals is via self-epitaxial nucleation. This belongs to a special type of 3D nucleation, and there is a 3D nucleation barrier ($\Delta G^*_{\text{mis}}$) associated with it. For such a process, suppose there are two events of *the self-epitaxial nucleation* occurring at the same site, one with a poor structural match ($\Delta G^*_{\text{mis}}$) and the other with a good structural match ($\Delta G^{*\prime}_{\text{mis}} = f_{\text{match}}(m)\Delta G^*_{\text{mis}},\ f_{\text{match}}(m) \ll 1$) as shown in Fig. 7.13b. Due to the high nucleation barrier at low supersaturations, it is very difficult for the mismatch epitaxial nucleation to occur as $\Delta G^*_{\text{mis}}$ is very high (i.e., (7.16) and Fig. 7.13b). Under such conditions, only the epitaxial nucleation with a good structural match may occur, as the good structural match substantially lowers the nucleation barrier (i.e., $f_{\text{match}}(m) \ll 1$, Fig. 7.13b). One has the formation of the ordered calcite crystallite assembly observed in Fig. 7.13a. As the supersaturation increases, the nucleation barrier for mismatch epitaxial nucleation $\Delta G^*_{\text{mis}}$ drops rapidly (Fig. 7.13b). At relatively high supersaturations, the requirement of adopting the good structural match between the daughter crystals and the substrates becomes less demanded, in the view of a low nucleation barrier $\Delta G^*_{\text{mis}}$. Due to the shadow effect, the mismatch self-epitaxial nucleation becomes kinetically more favorable. The shadow region in Fig. 7.13b illustrates the region the mismatch self-epitaxial nucleation may occur. This facilitates self-epitaxial nucleation leading to formation of the assembly of HAP crystallites with small mismatch (see Fig. 7.13a,b). As the supersaturation increases further, the nucleation barrier for mismatch epitaxial nucleation totally collapses. Self-epitaxial nucleation occurs much more easily, resulting in a severe interfacial structural mismatch. In this case, the crystallite assembly will often be randomly and highly branched (see Fig. 7.13a,b). This causes the *supersaturation-driven interfacial structural mismatch*.

As indicated above, as $\sigma$ progressively increases from low supersaturations to high supersaturations, the self-epitaxial nucleation will be governed by a sequence of progressive heterogeneous processes associated with increasing $f(m)$. In analogy with the above analysis, the biomineralization of HAP in simulated body fluids was carried out [84]. Correspondingly, we should obtain a set of pairwise intersecting straight lines if $\ln t_s$ is plotted against $1/[\ln(1+\sigma)]^2$ ($t_s$: induction time; cf. Fig. 7.13c,d). Since for the crystalline phase, $m$, and $f(m)$ take on only those values that correspond to some crystallographically preferential orientations, $f(m)$ or the slope of the straight lines will take on discrete values, and $f(m)$ will increase as $\sigma$ increases.

As shown in Fig. 7.13c and d, the interfacial correlation factor $f(m,R')$ subsequently increases from $3.9/\rho$ to $12.5/\rho$, as supersaturation increases from 1.5 to 5. This result unambiguously confirms that the increase in supersaturation will drive the substrates/biominerals from an interfacial structural match state (a lower $f(m)$) to an interfacial structure mismatch state (a higher $f(m)$). The abrupt changes from one state to the other at certain supersaturations (such as A, B, . . . in Fig. 7.13d) are due to the anisotropy of the crystalline phase.

To explore the effects of *the self-epitaxial nucleation-induced assembly* and the *supersaturation-driven interfacial structural mismatch* at the single particle

level, controlled heterogeneous 2D colloidal crystallization experiments by the AE field can be applied again. The pre-defined 1D colloidal lines or lithographically templated electrodes (Fig. 7.14a) can be utilized to site-specifically initiate the 2D colloidal nucleation and control the crystal orientation, wherein controlling an external AEF (thermodynamic driving force) allows us to precisely and conveniently manipulate the kinetic process of the crystal growth. Here, the epitaxial assembly method based on the crystallization of 2D colloidal crystals under an AEF can be applicable to investigate this matter (Fig. 7.14).

To examine the ordering of the colloidal crystals at the template, the orientational order parameter $S = \frac{1}{2}\langle 3\cos^2\theta - 1\rangle$ [88] is applied to characterize the uniaxial ordering of the colloidal assembly. $\theta$ is the misfit angle of the crystal domain with respect to the epitaxial colloidal line, as shown in the right inset in Fig. 7.14b. The brackets denote an average over all of the particles in the assembly. When colloidal particles are perfectly oriented parallel to the epitaxial template, one has $S = 1$. Figure 7.14b shows the frequency dependence of the orientation order parameter of the colloidal crystals. The perfectly oriented single colloidal crystals are obtained in the low-frequency range (400–800 Hz, low-driving force regime). When the frequency increases to the high-frequency range (1,000–2,000 Hz, high-driving force regime), the degree of perfection gradually decreases [33, 35, 37, 39]. For 1.8 μm PS particles, the interparticle separation $r_{eq}$ among the assembly decreases with increasing frequency from 400 to 1,000 Hz and then reaches its minimum in the frequency range of 1,000–2,000 Hz, as shown in Fig. 7.14c. This suggests that the attractive forces among the particles become more dominant with increasing frequency and are much stronger than the repulsive ones in the frequency range of 1,000–2,000 Hz. In the high-frequency range, the homogeneous nuclei are very tightly assembled. Hence, the conformations and orientations of the homogeneous nuclei are difficult to be rearranged by the attractions from the template when they approach the template. Therefore, the degree of perfection of the colloidal crystals decreases in the frequency range of 1,000–2,000 Hz. On the other hand, the nucleation rate, in the bulk fluid phase, is large because of the increased attractive forces in the high-frequency range (Fig. 7.14c). Due to the increase in the homogeneous nucleation rate, the entropy effect and the transport will result in a certain degree of randomness [88]. This will lead to a reduction of interfacial correlation between the template and the incoming growth units and, thus, a decrease in the degree of perfection of the colloidal crystals and the mismatch with the template, which can be considered as the verification of the *supersaturation-driven interfacial structural mismatch* effect.

Note that the self-epitaxial nucleation-induced assembly and the supersaturation-driven interfacial structural mismatch will explain not only the pattern formation in biomineralization, but also the influence of $F^-$ in the hard tissue formation [86]. In the field of materials engineering, by carefully adjusting these two effects, one can engineer and fabricate the complex structures of functional materials at the micro/nanostructural level.

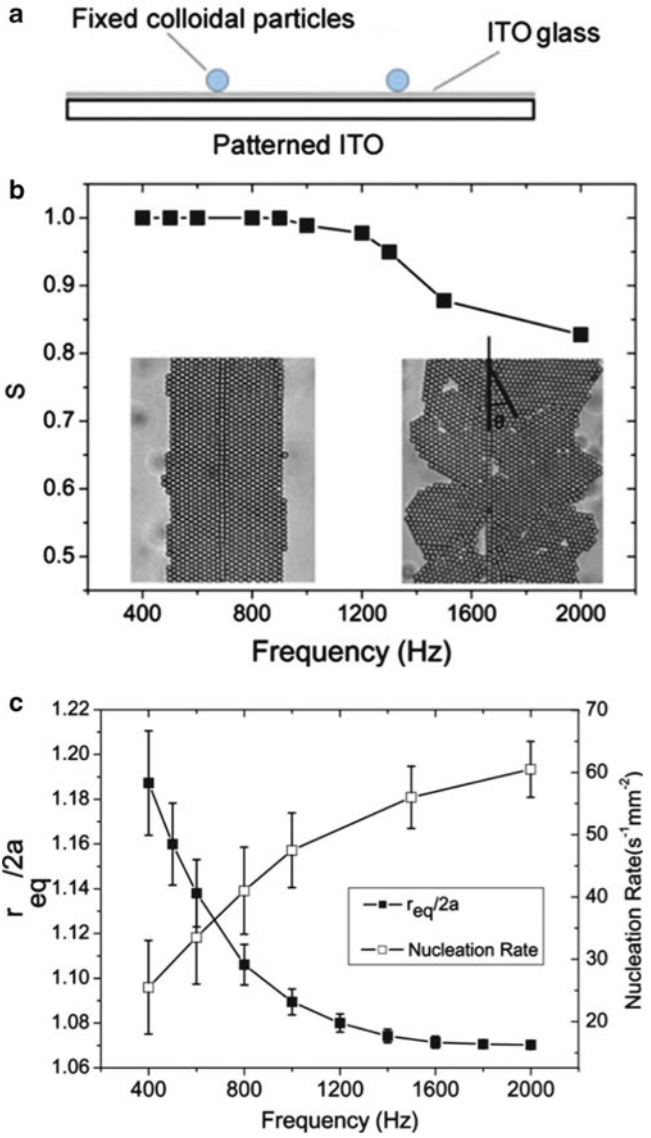


**Fig. 7.14** (**a**) Schematic illustration of experimental setup for heterogeneous 2D colloidal crystallization experiments under an AEF. Refs. [39–42]. (**b**) Frequency dependence of the orientational order parameter $S$ under an AEF. Also shown are the optical images of a perfectly oriented colloidal crystal (*left* inset, $S = 1$) and a roughly oriented colloidal crystal (*right* inset, $S = 0.83$), assembled at 800 Hz and 2,000 Hz for 10 min, respectively. (**c**) Variation of $r_{eq}/2a$ and nucleation rate in the bulk fluid phase with frequency for 1.8 μm PS particles. Reproduced with permission from Ref. [31] ©2009 American Chemical Society

## 7.4 Photonic Crystals and Biomimetics of Butterflies' Wings Crystals

Apart from the advancing of our knowledge in crystallization, colloidal crystallization has a wide range of applications in different areas. Among these, fabricating photonic crystals is one of the most important applications. The periodic modulation of the refractive index in a dielectric material creates a forbidden gap in the photonic band structure, which is not allowed in the existence of optical modes within a specific range of frequencies. Such photonic band-gap materials, known as photonic crystals, are attractive optical materials for controlling and manipulating light. In the last decades, a number of methods have been developed to fabricate photonic crystals at various length scales, including layer-by-layer stacking techniques using microfabrication tools [89–91], electrochemical etching [92, 93], laser-beam-scanning chemical vapor deposition [94], and holographic lithography [95, 96]. Colloidal crystal, in which the periodic modulation of the dielectric constant is realized by self-assembling monodisperse colloidal objects such as silica ($SiO_2$) or polystyrene (PS) microspheres into ordered arrays, turns out to be an effective approach to photonic crystal preparation [97–100]. The resulting photonic properties are determined by the symmetry and lattice constant of the crystal and the refractive index contrast between the colloids and the surrounding medium. The sizes of colloids are typically in the range of 100 nm to several micrometers. The self-assembly and fabrication of 2D/3D colloidal crystals have attracted broad interest because of their wide applications in photonic crystals [26, 101–103], chemical and biochemical sensors [28, 104], optoelectronic devices [105, 106], and templates for colloidal nanolithography [107].

### *7.4.1 Fabrication of 2D Colloidal Crystals and Templating*

The commonly used methods to fabricate self-assemble monodispersed colloidal particles into ordered 2D arrays are based on the lateral capillary interaction, which originates from the deformation of the liquid surface [108–111]. The colloidal particles are typically assembled at the air–liquid interface or in a thin liquid layer supported on a flat, clean, and chemically homogeneous solid substrate in terms of the surface pressure and convection [112–117]. Another method to create 2D arrays is electrophoretic deposition, which applies a strong electric field to assemble colloidal dispersions confined between two parallel solid electrodes as outlined above [31, 37–46].

To achieve practical applications, two major obstacles need to be overcome in fabricating 2D colloidal crystal. First, many applications for colloidal crystals require samples that are free from defects over large length scales. However, most self-assembly systems suffer from disorders resulting from homogeneous nucleation and uncontrollable crystal growth. Second, the introduction of well-defined artificial

defects within colloidal crystals is another prerequisite for some practical applications [118]. Linear defects, for instance, could be used as photonic waveguides and point defects as microcavities [105]. However, this cannot be achieved through conventional self-assembly methods alone, as the intentionally added defects will substantially frustrate the crystal growth and locally induce disordering in colloidal crystals [119]. Experimentally, a key challenging of controlling colloidal crystals is lack of reliable methods to control colloidal crystallization of large and perfect single crystals with predefined orientations, artificial defects, and patterns over fast time scales. Obviously, the electrically controlled 2D colloidal crystallization is one of the most promising technologies to acquire large and perfect 2D crystals based on the principles outlined in Sect. 7.3.5.

### *7.4.2 Fabrication of 3D Photonic Crystals*

The technologies adopted to fabricate the 2D colloidal crystals can be extended to fabricate 3D colloidal crystals with some modifications. Several other methods have also been widely employed to assemble highly ordered 3D crystals with large domain size, including sedimentation, repulsive electrostatic interactions, and physical confinement. Among these, sedimentation in a gravitational field seems to be the simplest approach for building 3D colloidal crystals [120]. A number of parameters must be carefully controlled to grow colloidal crystals of high quality. These parameters include the size, uniformity, and density of the colloids, as well as the rate of sedimentation. The main disadvantages of this method are the poor control over the structure and the thickness of the crystalline arrays, the long preparation time, and the polycrystalline nature of the products. Highly charged colloidal particles suspended in a solution can spontaneously self-organize into ordered structures, driven by the minimization of electrostatic repulsive interactions [121–125]. The colloidal crystals prepared using this method are typically non-close-packed, because the repulsive electrostatic interactions keep the particles away from each other. This method has very strict requirements regarding the experimental conditions such as the surface charge density, the colloidal concentration, and the ionic strength. By leaving the colloidal suspension to a physical confinement, it would self-assemble into long-range-ordered crystalline structures [126–128]. Colloidal crystals with domain sizes of square centimeters could be fabricated by using a specially designed packing cell [129–131]. This method is relatively fast, and it also provides tight control over the structures and the thickness of the 3D colloidal crystals.

### *7.4.3 Biomimetics of Structural Color*

Color production in the animal kingdom normally takes advantage of either pigmentation or structural coloration. Color produced from pigmentation is also called chemical color, which comes from the selective absorption of the incident light and the reflection from the remaining spectra of the light by pigments. Structural color, also called physical color, is caused by complicated interaction between light and microstructures with featured sizes comparable to the visible wavelengths [132]. In this case, fundamental optical processes such as reflection, refraction, interference, diffraction, and scattering are the basic physical origination of structural color. Comparing with the colors arising from pigments, structural colors possess many interesting features since it is produced structurally. Generally, structural color is of high brightness and saturation and is hence sometimes called metallic color. It may display iridescence [133], i.e., a color change with perspective. The variations of structures or contrast of refractive indices may alter structural color, which can be achieved by applying pressure or infiltrating liquids in air voids. In contrast to pigmentary coloration, structural color never fade away provided that the corresponding photonic structure retains unchanged.

In recent years, structural color and relevant photonic structure have been subjected to extensive studies because of their scientific and practical importance [132–139]. The study of structural color may render tremendous important information related from evolution, biological functions, structural formation, to strategies of light steering. On the other hand, structural color may have potential applications in a variety of industries including photonics, display, painting, and textile. Natural photonic structures and the ingenious ways of light steering may have been a great source of inspiration in our design and fabrication of new optical materials and devices for future technological applications.

A wide variety of structural colors can be found in nature, among which the most famous examples are vivid colors of some breeds of butterfly wings and peacock feathers [140–144]. Metallic reflection from the elytra of beetles and iridescent stripes in some kinds of fish are also typical natural structural colors [145–147]. As illustrated in Fig. 7.10a, the 2D photonic crystals in the cortex of different colored barbules are responsible for the coloration of peacock feather [140, 144], while the multilayer structures of wing scales produce the structural coloration of some breeds of butterflies [148].

#### 7.4.3.1 Applications of Colloidal Crystals in Mimicking of Structural Color

During the last two decades, much effort has been devoted to mimicking natural structural color, although to obtain the dedicated structures with the structural color as seen in animal kingdom (Fig. 7.15a) remains to be a big challenge. One way to acquire structural color was to adopt the nature structural color materials as

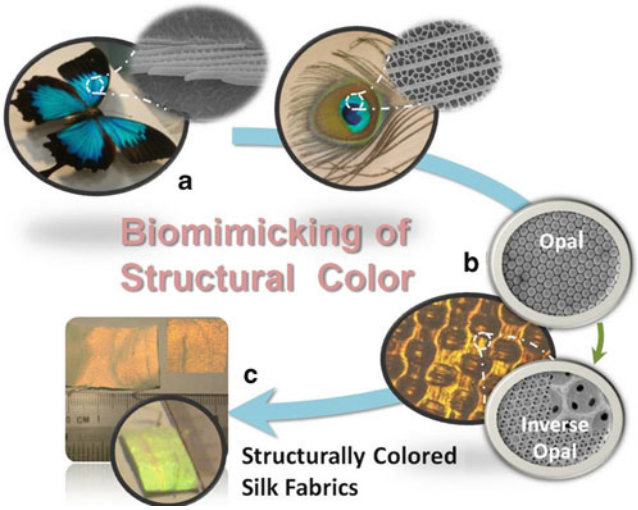


**Fig. 7.15** Biomimetics of structural colors on silk fabrics. (**a**) The structural colors of butterfly (*Papilio ullysess* butterfly) and peacock feather. (**b**) Fabrication of opal and inverse opal on silk fabrics. Refer to Ref. [140] for the details of fabrication. (**c**) Structurally colored silk fabrics. Reprinted with permission from Ref. [30] © 2012 Wiley-VCH Verlag GmbH & Co

templates to replicate the nanostructures so as to obtain the optical properties. Wang *et al.* examined the fine structure of the wing scale of a *Morpho peleides* butterfly and replicated the entire configuration by a uniform $Al_2O_3$ coating through a low-temperature atomic layer deposition (ALD) process [149]. An inverted structure was achieved by removing the butterfly wing template at high temperature, forming a polycrystalline $Al_2O_3$ shell structure with precisely controlled thickness. Other than the copy of the morphology of the structure, the optical property, such as the existence of photonic band gap (PBG), was also inherited by the alumina replica. Other replicating methods have also been employed to replicate the structures of natural photonic materials, including conformal-evaporated-film-by-rotation technique and soft lithography technique [150, 151].

3D colloidal crystals with a PBG lying in the visible range are another option for mimicking natural structural color. Inspired by natural photonic crystals (Fig. 7.15), researchers have fabricated colloidal crystals with tunable structural colors [152–158]. One of the most commonly used techniques to fabricate colloidal crystals is the evaporation-induced self-assemble method, which enables the rapid production of highly ordered 3D colloidal crystals with face-center cubic structure. In connection with this technology, the wettability can be adjusted by the intrinsic roughness of colloidal crystals in combination with the tunable chemical composition of latex surfaces while the band gaps can be tuned by changing the size of the colloidal spheres.

Although colloidal crystals can be fabricated easily and are of wide potential applications, they are weak in the mechanical properties and dispersible in water.

Practically, the applications require colloidal crystals to be either fixed or replicated by other more robust materials [158–163]. Alternatively, one can replicate the colloidal crystal structure using a durable material, creating an inverse opal structure. In this regard, colloidal crystals serve as the templates, with the voids infiltrated by a material that solidifies in place without disrupting the order of the crystals. The original colloidal particles are subsequently removed, leaving behind an inverted structure of the colloidal crystals. The method has by now been used to make highly ordered porous materials from a wide variety of precursors and templates. By adjusting the dimension of the pores, as well as the refractive index of the material, PBG of the inverse opal structure can be tuned accordingly.

Another important property that can be seen in nature is tunable structural color, such as the color change that can be seen on the surface of a damselfish [164]. In order to mimic such color change, several methods have been developed to create tunable structural color films. Responsive photonic crystals (RPCs) are materials with photonic band-gap properties that can be tuned by external stimuli. To create such materials, a stimulus–response mechanism needs to be coupled with the photonic crystal structure [165]. There are generally two approaches to introduce such responsive materials. In the first case, the responsive materials are directly prepared in the form of building blocks that can be used for constructing photonic crystals. A typical example is the 1D Bragg stacks formed by self-assembly of block copolymers that contain segments that can expand when exposed to certain solvents. In the second case, the periodic structures are defined first, and then the responsive materials are filled into the interstitial space to form a composite material that is optically tunable and mechanically stable [166–171]. If the responsive material cannot provide enough mechanical strength, an inverse opal structure will be formed by first infiltrating an inert material into the interstitial space of the periodic structure to form a robust framework and then removing the original periodic template through calcination or chemical etching. Finally, the responsive materials are filled into the porous structure of the inverse opals. In the second case, the responsibility of nature structural color was mimicked by fabricating various RPCs (thermal, chemical, optical) based on colloidal crystals and templating.

To create structural colors on fabrics is extremely important, practically, but remains as a challenging task. As color fading caused by leaching or oxidation/bleaching is a key issue in fabric care, producing with vivid and durable structural colors on fabrics by fabricating the 3D colloidal crystals onto the surface of fabrics will revolutionize textile and fashion industries [158]. If the physical structure of photonic crystals on the fabrics is strong enough, the colors will last forever. Recently, a combined surface treatment technology [158] allows us to create opal and/or inverse opal structures on silk fabrics (cf Fig. 7.15). In producing structural colors on silk fabrics, polystyrene spheres with different diameters were assembled on the surface of silk fabrics. Silk fibroin was dispersed on the colloidal crystals as binding materials (Fig. 7.15b). Thus, silk fabrics with different reflection peaks ranging from ultraviolet to near-infrared can be obtained. It follows that the colors (the reflected wave lengths) can be created by tuning the lattice constant of

the inverse opal, $a$, according to $\lambda = va$ ($v$: a function of the refractive index of the material) [152–158].

Furthermore, multifunctional silk fabrics may also be obtained by controlling the band gaps of the photonic crystals. For example, one can acquire the UV protective clothing by creating photonic crystals or inverse capable of reflecting UV light. On one hand, the thermal insulating performance due to a reflection peak in the IR range will create cooling textiles in a hot summer. On the other hand, it will preserve to some extent our body heat in a cold winter if the IR reflecting structure is generated in the inner layer of textiles.

#### 7.4.3.2 Double Reflection of Structural Color by Surface Structural Engineering

Although great accomplishment has been made, the structural colors produced by the animal kingdom are much richer and more effective than what we can produce so far. Furthermore, it is especially difficult to mimic some unique optical properties of natural structural color, such as polarization, colors mixing, etc. In the following, we will describe the double reflection and polarization effect produced by *Papilio* butterfly and a method utilizing a combined colloidal crystal and surface deposition technique to mimic these effects.

Apart from the iridescent visibility, nature structural color produced by some animals also gives rise to additional unique optical properties and benefits. For instance, the brown barbules in male peacock tail feathers adopt mixed structural coloration [140], Some breeds of *Papilio* butterflies reveal the double reflection effect [141, 172].

The color mixing mentioned above is created by in nature in different ways [173]. Figure 7.16a depicts the double reflection and iridescent visibility created by the blue wing scales of *Papilio ulysses*. The surface of its wings is composed of millions of scales. The scales of *P. ulysses* are of a size around 150 μm × 90 μm and consist of a fairly regular array of concavities. Under optical microscope, the concavities reveal a green reflection light (Fig. 7.11a(i)). When illuminated and observed at normal incident light, the concavities in *P. ulysses* appear to be green (Fig. 7.16a(i,ii)). However, upon crossing an input linear polarizer with an exit analyzer, the green reflected light in *P. ulysses* almost disappear while the deep purple (near-UV) color reflected by ridges in *P. ulysses* reflect back (Fig. 7.16a(iii) & (iv)). This implies that the purple reflected light is not altered by the polarizers. By further characterization of the microstructures of the wing scales, it was found that the profile of the concavities was almost flat, the ridges run through the full length of the scales with a periodicity of 4–5 μm (Fig. 7.16a(iv)). The configuration of the ridges is a 2D array of 70 nm×100 nm rectangular air squares surrounded by organic cuticle layers (the main and sub-ribs) with a periodicity of 140 nm ($D_1 + d_1$) along its length direction and 160 nm ($D_2 + d_2$) along the main ribs. This long-range ordered structure with a very small periodicity can be considered to be a 2D photonic crystal slab tilt about 30° with respect to the surface of the scales.

As shown in Fig. 7.16a(v), the transverse cross section of the wing scales consists of 21 alternative cuticle and air layers, which share almost the same thickness ( 95 nm). The multilayer structure of the concavities (Fig. 7.16a(iii)) produces the green reflection light and gives rise to a main reflection peak at 550 nm for normal incident light. The 2D photonic crystal slab of the ridges tilts 30° to the surface of scales, interacting with the normal incident light at 60° and producing a small reflection located at 380 nm. Under 45° incident light, the main reflection peak produced by concavity blue-shifts to 350 nm; the ridges interact with the incident light at 15° and give rise to the small reflection peak at 550 nm. Therefore, the two spectra peaks originating from the concavities and the ridges could be observed for both normal and 45° incident light. The shifting of peaks suggests the iridescent property of structural color for *P. ulysses*. These two reflection peaks mix to the blue color perceived by human eyes.

The bright green-colored wings of *P. blumei* (Fig. 7.16b, another breed of *Papilio* butterfly) result from a juxtaposition of blue and yellow-green light reflected from different microscopic regions on the wing scales. Optical microscopy reveals that these regions are the centers (yellow) (Fig. 7.16b(ii)) and the edges (blue) of concavities (Fig. 7.16b(iii)). Unlike *P. ulysses*, the concavities of *P. blumei* are cap shaped, of 4–6 μm in diameter (Fig. 7.11b(vi)). The profile is much deeper than *P. ulysses*. The inclined sides of each concavity tilt 45° with respect to the horizontal surface, and the opposites of each concavity are perpendicular to each other. The ridges run through the full length of each scale with a periodicity of 7–8 μm. The transverse cross section of the concavities also consists of 21 alternative cuticle and air layers with a thickness around 110 nm (Fig. 7.16b(v)). For the normal incident light, theoretical calculation predicts that the reflection peak resulted from the flat portions locates at 600 nm, in agreement with the yellow color observed under optical microscopy, while the light incident on the edges of concavities with an angle 45°, producing a reflection peak at 450 nm, in accordance with the blue color observed under optical microscope. The light incident on one side of the concavity, reflected from one 45° side, travels across the concavity to the opposite orthogonal side and then reflects backward in parallel to the original incident direction. Through this double reflection process, the blue reflected light undergoes a polarization conversion. As a result, it survives upon the crossed polarizers. Under 45° incident light, the reflection peak arising from the flat portions is 450 nm (blue color) (Fig. 7.16b(iii), right), while the light is incident normally on the inclined sides and gives rise to a reflection peak located at 600 nm (yellow color) (Fig. 7.16b(ii), left). Therefore, for normal and 45° incident light, the cap-shaped concavities produce both yellow and blue colors. These two colors mix up to the green coloration caught by human eyes. It follows that the two breeds of butterfly take advantage of the color-mixing strategy. The blue color of *P. ulysses* is mixed by the green and deep purple colors reflected by concavities and ridges, respectively. The green color seen from *P. blumei* is a mixture of yellow and blue colors reflected by the flat portions and inclined sides of concavities, respectively. We notice that many studies show that the eyes of the butterflies have a duplicated gene, allowing them to see ultraviolet colors and distinguish the spectral properties and spatial

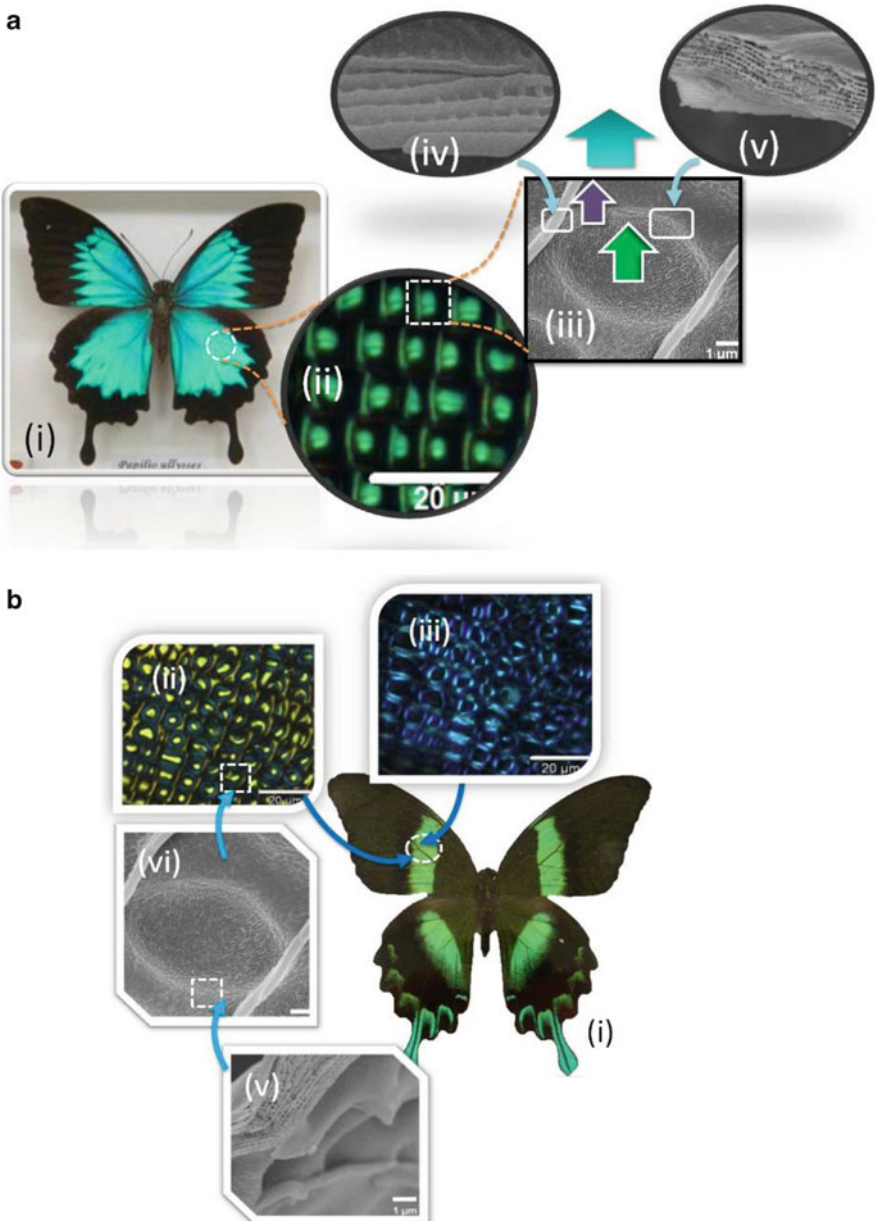


**Fig. 7.16** Biomimetics of structural colors by structural engineering. (**a**) Nature photonic structure, *Papilio ulysses* butterfly. (*i*) The *bright blue* wings of *P. ulysses* butterfly resulted from the mixed colors from different regions of the scales. (*ii*, *iii*) Optical and scanning electronic micrographs (scale bar: 20 μm) showing that the surface of a wing scale of a fairly regular array of concavities and ridges (*iv*). The concavities reflect *green color* light. (*iv*) UV light reflected from the ridges. (*v*) The transverse cross section of concavities of 21 alternative cuticle and air layers with a thickness of 95 nm, which reflect green light consistently (Ref. [148]).

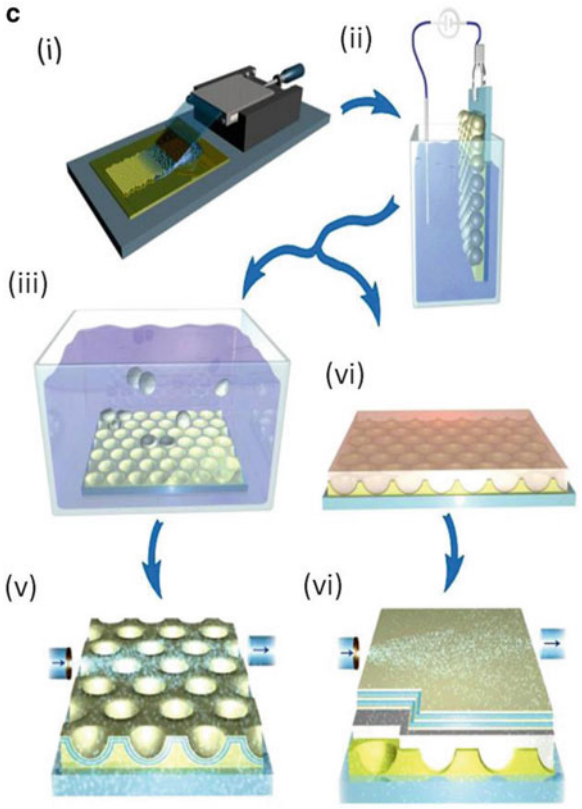


**Fig. 7.16** (continued) (**b**) Natural photonic structure, *Papilio blumei* butterfly. (*i*) The bright green wings of the *P. blumei* butterfly resulted from the mixing of the different *colors* of light from different regions of the wing scales. (*ii*, *iii*), Optical micrographs (scale bar: 20 μm) showing that the concavities reflect *yellow* and *blue colors* under normal incident light. (*vi*) Scanning electron micrograph showing that the surface of a wing scale is covered with concavities (diameter ≈ 5–10 μm). (*v*) The transverse cross section of concavities consists of 21 alternative cuticle and air layers with a thickness of 120 nm. Reflectance spectra under normally incident light and 45° incident light, and the overlapping of the spectra confirm the non-iridescent property of the green wing scales of *P. blumei* (From [148]). (**c**) Mimicking by surface structural engineering. (*i*) Deposition of polystyrene colloids on a gold-coated silicon substrate. (*ii*) Growth of platinum or gold in the interstices of the colloidal array by electroplating. The metal deposition is terminated when the thickness of the deposited film equals the microsphere radius. (*iii*) Removal of the polystyrene spheres from the substrate by ultrasonication in acetone. (*iv*) Sputtering of a thin carbon film and ALD of a stack of 11 alternating $TiO_2$ and $Al_2O_3$ layers (*arrows* indicate the precursor gas flow). (**e**, **f**) In a second route, the colloids are molten to cover the cavities with a homogeneous film, (*v*) which is covered by a $TiO_2$–$Al_2O_3$ multilayer [141] (*vi*). (**a**, **b**) Reprinted with permission from [30] © 2012 Wiley-VCH Verlag GmbH & Co. (**c**) Reprinted with permission from [172] ©2010, Nature publishing group

distribution of the visual colors [174]. And also, they are sensitive to the polarized light. Therefore, the knowledge on the structural origination of the two reflection peaks and polarization property of butterfly wings would have broad biological implications [175, 176]. Furthermore, with the understanding of the correlation between the optical properties and the corresponding structures, researchers could be able to find a way to mimic natural structural colors with designated properties. Evidently, the ability to mimic the structural color with its spectacular function will broaden the biomimicry field in the design of structural color materials targeted for ultra and smart performance.

Kolle et al. adopted the combined techniques of colloidal crystal self-assembly, sputtering, and ALD to fabricate photonic structures that mimic the color mixing and polarization effect found on the colored wing scales of *P. blumei* [172]. They demonstrated the replication of the periodically shaped multilayer structure of the *Papilio* butterfly scale in five steps (Fig. 7.16c). Polystyrene colloids with a diameter of 5 μm were assembled on a gold-coated silicon substrate to create regularly arranged concavities. A layer of platinum or gold with thickness 2.5 μm was then electrochemically grown into the interstitial space between the colloids, creating a negative replica [177–179]. Ultrasonication of the sample in dimethylformamide or acetone removed the colloids, resulting in a template of hexagonally arranged metal concavities. An 20-nm-thick carbon film was sputtered onto the gold surface. Finally, a conformal multilayer of thin quarter-wave titania and alumina films was grown by ALD [180]. The carbon layer between the gold (or platinum) and the multilayer stack adsorbs light passing through the multilayer stack, reducing specular reflections and unwanted destructive interferences that would otherwise severely limit the optical performance.

During the fabrication process, the diameter and the height of the concavities for the artificial mimic were well controlled by the size of colloidal spheres and thickness of platinum or gold layer. The number of the alternating titania and alumina layers, as well as their thicknesses, could be carefully controlled during the ALD process. By choosing proper thicknesses of the titania and alumina layers, the stop-band center wavelength for the artificial multilayer structure could locate 550 nm, matching the reflectance band of the natural *P. blumei* structure closely. Due to the concave structure, the center of the concavities exhibit yellow-green reflection ( 550 nm), while the reflection light from the four segments of the concavities blue-shifts to blue color. The observation of the artificial mimic between crossed polarizers leads to a similar effect as described for the *P. blumei* structure. Only light incident onto four segments of the concavity edges is detected. The local surface normal of 45° gives rise to a double reflection at the opposing cavity walls, causing a polarization rotation. The artificial mimic therefore displays the same optical characteristics as the natural *P. blumei* wing scale structure.

Nevertheless, this approach described above needs to fabricate complex nanostructures, wherein the two reflections come from different parts of the structure. This technique is costly and difficult to obtain different properties by tuning the structure. In this regard, the key challenges in future work to biomimic natural structural color turn out to be how to design and fabricate photonic crystals with the

unique optical properties of natural structural color through a simple process. One promising way is to construct photonic crystals with two PBGs to get the desired double reflection. On the other hand, the growing demand for optical interfaces and sensors for biomedical applications is a motivating research toward realizing biocompatible photonic components that offer a seamless interface between the optical and biological worlds. Therefore, another key issue in this field is how to mimic the double reflection effect using biocompatible and biodegradable materials.

We notice that the double reflection has its biological function. For instance, there are three major photoreceptors in the compound eyes of *Heliconius erato* with spectral sensitivity peaks at 370, 470, and 560–570 nm, allowing the detection of ultraviolet colors, and they distinguish the spectral properties of visible light [175]. It follows that the double reflection of butterfly wings giving rise to both visible and UV reflections may serve for communication and mating signals in butterfly kingdom [174–176]. Thus, investigating the correlation between the optical properties and the structures may help to explain the innate behaviors of the butterfly kingdom. Investigating the coloration mechanisms of these optical properties and the corresponding structures also has crucial implications for biomimicry, including color-stimulus synthesis, display technologies, and various polarization applications [116, 181].

## 7.5 Conclusive Remarks

As can be seen from the results presented in this chapter, almost all fundamental aspects of crystallization in biomineralization can be examined in terms of the AEF-controlled 2D colloidal crystallization system. For instance, the initial stage of nucleation may not be exactly the same as we expected. Unlike the assumption that both the embryos and the bulk crystals share the same structure, the structures of the embryos are supersaturation dependent. Such a deviation would be beneficial in lowering the nucleation barrier and then facilitating the nucleation kinetics at low supersaturations. From the point of view of solid–fluid interface, the above "experimental modeling" can also provide some unique and extremely relevant information, which is capable of updating our knowledge in crystallization in general. Notice that the effect of supersaturation-driven structure mismatch has been put forward, but never been visualized directly before. The templated 2D colloidal nucleation provides the first observation of this effect. Such an experimental modeling system has been successfully applied to examine many other crystallization processes, i.e., MSC, roughening transition, adatomic step integration, defects generation and migration kinetics, etc., which have never been examined quantitatively before at the single particle level. Note that the key advantage of the experimental modeling system is the combination of the visualization and the quantitative treatment, which can transfer our knowledge to a new phase. As the colloidal crystallization system displays the phase behaviors similar to normal crystalline materials, and the crystallization condition can be controlled easily and precisely, it can be foreseen that this approach will become a powerful tool to study the science and technology

of crystallization. In the area of application, apart from the fabrication of photonic devices, sensor, and tunable lasers, colloidal crystallization has been now applied to mimic the structural colors and double reflection on silk fabrics, which will exert a significant impact on textile, personal care, and fashion industries.

**Acknowledgements** The authors acknowledge the supports from Singapore ARC funding (Project No. T13-0602-P10).

## References

1. Gibbs, J.W.: Collected Works. Thermodynamics, vol. I. Longmans and Green, New York (1928)
2. Votmer, M., Weber, A.: Keimbildung in übersättigten Gebilden. Z. Phys. Chem. **119**, 277 (1926)
3. Farkas, L.: The speed of germinitive formation in over saturated vapours. Z. Phys. Chem. **125**, 236–242 (1926)
4. Kaischew, R., Stranski, I.: On the kinetic deflection rate of germ formation. Z. Phys. Chem. B **26**, 317–326 (1934)
5. Becker, R., Doering, W.: Kinetic treatment of germ formation in supersaturated vapour. Ann. Phys. **24**, 719–752 (1935)
6. Zeldovich, J.B.: On the theory of new phase formation, cavitation. Acta Physicochim. U.R.S.S. **18**, 1–22 (1943)
7. Hirth, J.P., Pound, G.M.: Progress in Materials Science: Condensation and Evaporation, vol. 2. Pergamon, Oxford (1963)
8. Nielsen, A.E.: Kinetics of Precipitation. Pergamon, Oxford (1964)
9. Liu, X.Y.: From molecular structure of solid-liquid interfaces to nucleation kinetics: implications for nanostructure engineering. In: Liu, X.Y., De Yoreo, J.J. (eds.) Nanoscale Structure and Assembly at Solid-Fluid Interfaces, vol. 2, pp. 109–176. Springer, London (2004)
10. Vekilov, P.G., Galkin, O.: Fundamental aspects of nucleation theory revealed in experiments with protein solid phases (Chp 5). In: Liu, X.Y., De Yoreo, J.J. (eds.) Nanoscale Structure and Assembly at Solid-Fluid Interfaces, vol. 1, pp. 105–144. Springer, London (2004)
11. Gasser, U., Weeks, E.R., Schofield, A., Pusey, P.N., Weitz, D.A.: Real-space imaging of nucleation and growth in colloidal crystallization. Science **292**, 258 (2001)
12. Philpott, M.R.: Atomic scale modelling of the solid-liquid interface (Chp 1). In: Liu, X.Y., De Yoreo, J.J. (eds.) Nanoscale Structure and Assembly at Solid-Fluid Interfaces, vol. 1, pp. 1–55. Springer, London (2004)
13. Zhang, K.Q., Liu, X.Y.: In situ observation of colloidal monolayer nucleation driven by an alternating electric field. Nature **429**, 739–743 (2004)
14. Hirtzel, C.S., Rajagopalan, R.: Invited review stability of colloidal dispersions. Chem. Eng. Commun. **33**, 301–324 (1985)
15. Evans, D.F., Wenneerstrom, H.: The Colloidal Domain: Where Physics, Chemistry, Biology, and Technology Meet. Wiley-VCH, Weinheim (1984)
16. Bradley, J.S.: The chemistry of transition metal colloids (Chp 6). In: Schmid, G. (ed.) Clusters and Colloids, pp. 459–537. Wiley-VCH, Weinheim (1994)
17. Ostwald, W.: Studien uber die Bildung und Umwandlung fester Korper. Z. Phys. Chem. **22**, 289 (1897)
18. ten Wolde, P.R., Frenkel, D.: Homogeneous nucleation and the Ostwald step rule. Phys. Chem. Chem. Phys. **1**, 2191–2196 (1999)
19. Poon, W.: Colloids as big atoms. Science **2004**(304), 830–831 (2004)
20. Frenkel, D.: Playing tricks with designer "Atoms". Science **2002**(296), 65–66 (2002)

21. Anderson, V.J., Lekkerkerker, H.N.W.: Insights into phase transition kinetics from colloid science. Nature **416**, 811–815 (2002)
22. Nadal, F., Argoul, F., Hanusse, P., Pouligny, B., Ajdari, A.: Electrically induced interactions between colloidal particles in the vicinity of a conducting plane. Phys. Rev. E **65**, 061409 (2002)
23. Grier, D.G., Murray, C.A.: The microscopic dynamics of freezing in supercooled colloidal fluids. J. Chem. Phys. **100**, 9088–9095 (1994)
24. van Blaaderen, A., Wiltzius, P.: Real-space structure of colloidal hard-sphere glasses. Science **1995**(270), 1177–1179 (1995)
25. Kegel, W.K., van Blaaderen, A.: Direct observation of dynamical heterogeneities in colloidal hard-sphere suspensions. Science **2000**(287), 290–293 (2000)
26. Vlasov, Y.A., Bo, X.Z., Sturm, J.C., Norris, D.J.: On-chip natural assembly of silicon photonic bandgap crystals. Nature **414**, 289–293 (2001)
27. Cheng, W., Wang, J., Jonas, U., Fytas, G., Stefanou, N.: Observation and tuning of hypersonic bandgaps in colloidal crystals. Nat. Mater. **5**, 830–836 (2006)
28. Holtz, J., Asher, S.A.: Polymerized colloidal crystal hydrogel films as intelligent chemical sensing materials. Nature **389**, 829–832 (1997)
29. Lawrence, J.R., Ying, Y., Jiang, P., Foulger, S.H.: Dynamic tuning of organic lasers with colloidal crystals. Adv. Mater. **18**, 300–303 (2006)
30. Diao, Y.Y., Liu, X.Y.: Controlled colloidal assembly: Experimental modeling of general crystallization and biomimicking of structural color. Adv. Func. Mater. **22**, 1354–1375 (2012)
31. Xie, R.G., Liu, X.Y.: Controllable epitaxial crystallization and reversible oriented patterning of two-dimensional colloidal crystals. J. Am. Chem. Soc. **131**, 4976–4982 (2009)
32. Everett, D.H.: Basic Principles of Colloidal Science. The Royal Society of Chemistry, Cambridge (1998)
33. Liu, Y., Narayanan, J., Liu, X.Y.: Colloidal phase transition driven by alternating electric field. J. Chem. Phys. **124**, 124906–124911 (2006)
34. Zhang, T.H., Liu, X.Y.: Configurations and diffusion of point defects in two-dimensional colloidal crystals. Appl. Phys. Lett. **89**, 261914 (2006)
35. Liu, Y., Liu, X.Y., Narayanan, J.: Kinetics and equilibrium distribution of colloidal assembly under an alternating electric field and correlation to degree of perfection of colloidal crystals. J. Phys. Chem. C **111**, 995 (2007)
36. Zhang, T.H., Liu, X.Y.: Effect of long-range attraction on growth model. J. Phys. Chem. C **111**, 1342–1346 (2007)
37. Zhang, K.Q., Liu, X.Y.: Size-dependent planar colloidal crystals guided by alternating electric field. Appl. Phys. Lett. **90**, 111911 (2007)
38. Zhang, K.Q., Liu, X.Y.: Two scenarios of the colloidal phase transitions. Phys. Rev. Lett. **96**, 105701–105704 (2006)
39. Liu, Y., Xie, R.G., Liu, X.Y.: Fine tuning of equilibrium distance of two-dimensional colloidal assembly under an electric field. Appl. Phys. Lett. **90**, 063105 (2007)
40. Zhang, T.H., Liu, X.Y.: How does transient amorphous precursor template crystallization. J. Am. Chem. Soc. **129**, 13520–13526 (2007)
41. Zhang, T.H., Liu, X.Y.: Multistep crystal nucleation: a kinetic study based on colloidal crystallization. J. Phys. Chem. B **111**, 14001–14005 (2007)
42. Xie, R.G., Liu, X.Y.: Electrically directed on-chip reversible patterning of two-dimensional tunable colloidal structures. Adv. Funct. Mat. **18**, 802–809 (2008)
43. Xie, R.G., Liu, X.Y.: Epitaxial assembly and ordering of two-dimensional colloidal crystals. Appl. Phys. Lett. **92**, 083106 (2008)
44. Zhang, T.H., Liu, X.Y.: Nucleation: what happens at the initial stage? Angew. Chem. Int. Ed. **48**, 1308–1312 (2009)
45. Zhang, K.Q., Liu, X.Y.: Controlled formation of colloidal structures by an alternating electric field and its mechanisms. J. Chem. Phys. **130**, 184901–7 (2009)
46. Zhang, K.Q., Liu, X.Y.: Determination of elastic constants of two-dimensional close-packed colloidal crystals. Langmuir **25**, 5432–5436 (2009)

47. Trau, M., Saville, D.A., Aksay, I.A.: Field-induced layering of colloidal crystals. Science **272**, 706–709 (1996). Trau, M., Saville, D.A., Aksay, I.A.: Assembly of colloidal crystals at electrode interfaces. Langmuir **13** 6375–6381 (1997).
48. Yeh, S.R., Seul, M., Shraiman, B.I.: Assembly of ordered colloidal aggregates by electric-field-induced fluid flow. Nature **386**, 57–59 (1997)
49. Liu, X.Y.: Gleation with small molecules: from formation mechanism to nanostructure architecture. In: Sato, K., Nakajima, K., Furukawa, Y. (eds.) Advances in Crystal Growth Research, pp. 42–61. Elsevier Science B.V., Amsterdam (2001)
50. Liu, X.Y.: From template nucleation to functional materials engineering. In: Skowronski, M., DeYoreo, J.J., Wang, C.A. (eds.) Perspectives on Inorganic, Organic and Biological Crystal Growth: From Fundamentals to Applications, pp. 439–465. American Institute of Physics, Park City, Utah (2007)
51. Li, J.-L., Liu, X.Y. Architecture of supramolecular soft functional materials: from understanding to micro/nano engineering. Adv. Fun. Mat. **20** 3196–3216 (2010). Liu, X.Y.: Chapter 1. In: Frédéric, F. (ed.) Low Molecular Mass Gelators: Design, Self-Assembly, Function. Topics in Current Chemistry. Springer, Berlin, pp. 1–37 (2005).
52. Fowler, R., Giggenhein, E.A.: Statistical Thermodynamics. Cambridge University, London (2005)
53. Mutaftschiev, B.: Nucleation theory. In: Hurle, D.T.J. (ed.) Handbook on Crystal Growth, pp. 189–245. North-Holland, Amsterdam (1993)
54. Liu, X.Y.: Simulating 'atomic' processes of crystallization via controlled colloidal assembly. In Wang, M., Tsukamoto, K., Wu, D. (eds.) Selected Topics on Crystal Growth: 14th International Summer School on Crystal Growth. American Institute of Physics, Dalian, pp. 173–220 (2010). Chernov, A.A. Modern Crystallography III—Crystal Growth. Springer-Verlag, Berlin (1984).
55. Liu, X.Y., Du, N.: Zero-sized effect of nano-particles and inverse homogeneous-like nucleation: principles of freezing and antifreeze. J. Biol. Chem. **279**, 6124–6131 (2004)
56. Liu, X.Y.: A new kinetic model for 3D heterogeneous nucleation. J. Chem. Phys. **111** 1628 (1999). Liu, X.Y.: Heterogeneous nucleation or homogeneous nucleation? J. Chem. Phys. **112**, 9949–9955 (2000). Liu, X.Y., Maiwa, K., Tsukamoto, K.: Two-dimensional heterogeneous nucleation and the growth kinetics. J. Chem. Phys. **106** 1870 (1997)
57. Santana-Solano, J., Wu, D.T., Marr, D.W.M.: Direct measurement of colloidal particle rotation and field dependence in alternating current electrohydrodynamic flows. Langmuir **22**, 5932–5396 (2006)
58. Zettlemoyer, A.C.: Nucleation. Dekker, New York (1969)
59. Kashchiev, D.: The kinetic approach to nucleation. Cryst. Res. Technol. **19**, 1413–1423 (1984)
60. Lewis, B., Andersen, J.C.: Nucleation and Growth of Thin Films. Academic, New York (1978)
61. Lutsko, J.F., Nicolis, G.: Theoretical evidence for a dense fluid precursor to crystallization. Phys. Rev. Lett. **96**, 046102 (2006)
62. Navrotsky, A.: Energetic clues to pathways to biomineralization: Precursors, clusters, and nanoparticles. Proc. Natl. Acad. Sci. **101**, 12096–12101 (2004)
63. Pan, H., Liu, X.Y., Tang, R., Xu, H.: Mystery of the transformation from amorphous calcium phosphate to hydroxyapatite. Chem. Commun. **46**, 7415–7417 (2010)
64. Termine, J.D., Eanes, E.D.: Comparative chemistry of amorphous and apatitic calcium phosphate preparations. Calcif. Tissue Int. **10**, 171 (1972)
65. Bradt, J.H., Mertig, M., Teresiak, A., Pompe, W.: Biomimetic mineralization of collagen by combined fibril assembly and calcium phosphate formation. Chem. Mater. **11**, 2694–2701 (1999)
66. ten Wolde, P.R., Frenkel, D.: Enhancement of protein crystal nucleation by critical density fluctuations. Science **277**, 1975–1978 (1997)
67. Zhang, J., Liu, X.Y.: Effect of protein-protein interactions on protein aggregation kinetics. J. Chem. Phys. **119** 10972 (2003). Narayanan, J., Liu, X.Y.: Protein interactions in undersatu-

rated and supersaturated solutions: a study using light and X-ray scattering. Biophys. J. **84**, 523–532 (2003). Chow, P.S., Liu, X.Y., Zhang, J., Tan, R.B.H.: Spherulitic Growth Kinetics of Protein Crystals. Appl. Phys. Lett. **81**, 1995–1997 (2002)
68. Jia, Y.W., Liu, X.Y. Self-assembly of protein at aqueous solution surface in correlation to protein crystallization. Appl. Phy. Lett. **86**, 023903 (2005). Jia, Y.W., Narayanan, J., Liu, X. Y., Liu, Y.: Investigation of the mechanism of crystallization of soluble protein in the presence of nonionic surfactant. Biophys. J. **89** 4245–4251 (2005)
69. Wang, L., Liu, X.Y.: Kinetic analysis of protein nucleation in gel matrix. Biophys. J. **95**, 5931–5940 (2008)
70. Haas, C., Drenth, J.: The interface between a protein and an aqueous solution and its effects on nucleation and crystal growth. J. Phys. Chem. B **104**, 368–377 (2000)
71. Beniash, E., Aizenberg, J., Addadi, L., Weiner, S.: Amorphous calcium carbonate transforms into calcite during sea urchin larval spicule growth. Proc. R. Soc. Lond. Ser. B **264**, 461–465 (1997)
72. Addadi, L., Raz, S., Weiner, S.: Taking advantage of disorder: amorphous calcium carbonate and its roles in biomineralization. Adv. Mater. **15**, 959–970 (2003)
73. Chen, X., Samia, A.C.S., Lou, Y., Burda, C.: Investigation of the crystallization process in 2 nm CdSe quantum dots. J. Am. Chem. Soc. **127**, 4372–4375 (2005)
74. Kashchiev, D., Vekilov, P.G., Kolomeisky, A.B.: Kinetics of two-step nucleation of crystals. J. Chem. Phys. **122**, 244706 (2005)
75. Kuznetsov, Y.G., Malkin, A.J., McPherson, A.: The liquid protein phase in crystallization: a case study-intact immunoglobulins. J. Cryst. Growth **232**, 30–39 (2001)
76. Auer, S., Frenkel, D.: Line tension controls wall-induced crystal nucleation in hard-sphere colloids. Phys. Rev. Lett. **91**, 015703 (2003). Liu, X.Y., Bennema, P., van der eerden, J.P.: The rough-flat-rough transition at crystal surfaces. Nature **356**, 778 (1992)
77. Vekilov, P.G.: Dense liquid precursor for the nucleation of ordered solid phases from solution. Cryst. Growth Des. **4**, 671–685 (2004)
78. Kamat, S., Su, X., Ballarini, R., Heuer, A.H.: Structural basis for the fracture toughness of the shell of the conch Strombus gigas. Nature **405**, 1036–40 (2000)
79. Li, X., Chang, W.C., Chao, Y.J., Wang, R., Chang, M.: Nanoscale structural and mechanical characterization of a natural nanocomposite material: the shell of red abalone. Nano Lett. **4**, 613–617 (2004)
80. Weiner, S., Wagner, H.D.: The material bone: structure-mechanical function relations. Annu. Rev. Mater. Sci. **28**, 271–298 (1998)
81. Birchall, J.D.: In: Mann, S., Webb, J., Williams, R.J.P. (eds.) Biomineralization: Chemical and Biochemical Perspectives, p. 491. VCH, Weinheim (1989)
82. Gao, H., Ji, B., Jager, I.L., Arzt, E., Fratzl, P.: Materials become insensitive to flaws at nanoscale: Lessons from nature. Proc. Natl. Acad. Sci. U.S.A. **100**, 5597–5600 (2003)
83. Jiang, H.D., Liu, X.Y., Lim, C.T., Hsu, C.Y.: Ordering of self-assembled nanobiominerals in correlation to mechanical properties of hard tissues. Appl. Phys. Lett. **86**, 16391 (2005)
84. Liu, X.Y., Lim, S.W.: Templating and supersaturation driven anti-templating: principles of biominerals architecture. J. Am. Chem. Soc. **125**, 888–995 (2003). Liu, X.Y.: Effect of microgravity on Ca mineral crystallization and implications for osteoporosis in space. Appl. Phys. Lett. **79**, 3539–3541 (2001)
85. Jiang, H.D., Liu, X.Y.: Principles of mimicking and engineering the self-organized structure of hard tissues. J. Biol. Chem. **279**, 41286–41293 (2004)
86. Wang, Z.Q., Ma, G.B., Liu, X.Y.: Will fluoride toughen or weaken our teeth? J. Phys. Chem. B **113**, 16393–16399 (2009)
87. Liu, X.Y.: Interfacial effect of molecules on nucleation kinetics. J. Phys. Chem. B **105**, 11550–11558 (2001)
88. Liu, X.Y.: A new kinetic model for 3D heterogeneous nucleation. J. Chem. Phys. **111**, 1628 (1999)
89. Lin, S.Y., Fleming, J.G., Hetherington, D.L., Smith, B.K., Biswas, R., Ho, K.M., Sigalas, M.M., Zubrzycki, W., Kurtz, S.R., Bur, J.: A three-dimensional photonic crystal operating at infrared wavelengths. Nature **394**, 251–253 (1998)

90. Fleming, J.G., Lin, S.Y.: Three-dimensional photonic crystal with a stop band from 1.35 to 1.95 μm. Opt. Lett. **24**, 49–51 (1999)
91. Noda, S., Tomoda, K., Yamamoto, N., Chutinan, A.: Full three dimensional photonic bandgap crystals at near-infrared wavelengths. Science **289**, 604–606 (2000)
92. Birner, A., Wehrspohn, R.B., Gsele, U.M., Busch, K.: Silicon-based photonic crystals. Adv. Mater. **13**, 377–388 (2001)
93. Masuda, H., Ohya, M., Asoh, H., Nakao, M., Nohtomi, M., Tamamura, T.: Photonic crystal using anodic porous alumina. Jpn. J. Appl. Phys. **38**, L1403–L1405 (1999)
94. Wanke, M.C., Lehmann, O., Mller, K., Wen, Q.Z., Stuke, M.: Science **275**, 1284–1286 (1997)
95. Campbell, M., Sharp, D.N., Harrison, M.T., Denning, R.G., Turberfield, A.J.: Fabrication of photonic crystals for the visible spectrum by holographic lithography. Nature **404**, 53–56 (2000)
96. Shoji, S., Kawata, S.: Photofabrication of three-dimensional photonic crystals by multibeam laser interference into photopolymerizable resin. Appl. Phys. Lett. **76**, 2668 (2000)
97. Xia, Y., Gates, B., Yin, Y., Lu, Y.: Monodispersed colloidal spheres: old materials with new applications. Adv. Mater. **12**, 693–713 (2000)
98. Schroden, R.C., Al-Daous, M., Blanford, C.F., Stein, A.: Optical properties of inverse opal photonic crystals. Chem. Mater. **14**, 3305–3315 (2002)
99. Lpez, C.: Three-dimensional photonic bandgap materials: semiconductors for light. J. Opt. A **8**, R1 (2006)
100. Halaoui, L.I., Abrams, N.M., Mallouk, T.E.: Increasing the conversion efficiency of dye-sensitized $TiO_2$ photoelectrochemical cells by coupling to photonic crystals. J. Phys. Chem. B **109**, 6334–6342 (2005)
101. Judith, J.E.G., Vos, W.L.: Preparation of photonic crystals made of sir spheres in titania. Science **281**, 802–804 (1998)
102. Norris, D.J., Vlasov, Y.A.: Chemical approaches to three-dimensional semiconductor photonic crystals. Adv. Mater. **13**, 371–376 (2001)
103. Hynninen, A.P., Thijssen, J.H.J., Vermolen, E.C.M., Dijkstra, M., van Blaaderen, A.: Self-assembly route for photonic crystals with a bandgap in the visible region. Nat. Mater. **6**, 202–205 (2007)
104. Velev, O.D.E., Kaler, W.: In situ assembly of colloidal particles into miniaturized biosensors. Langmuir **15**, 3693–3698 (1999)
105. Joannopoulos, J.D., Villeneuve, P.R., Fan, S.: Photonic crystals: putting a new twist on light. Nature **386**, 143–149 (1997)
106. Yamasaki, T., Tsutsui, T.: Spontaneous emission from fluorescent molecules embedded in photonic crystals consisting of polystyrene microspheres. Appl. Phys. Lett. **72**, 1957 (1998)
107. Yang, S.M., Jang, S.G., Choi, D.G., Kim, S., Yu, H.K.: Nanomachining by colloidal lithography. Small **2**, 458–475 (2006)
108. Murray, C.A., VanWinkle, D.H.: Experimental observation of two-stage melting in a classical two-dimensional screened coulomb system. Phys. Rev. Lett. **58**, 1200–1203 (1987)
109. Bowen, W.R., Sharif, A.O.: Long-range electrostatic attraction between like-charge spheres in a charged pore. Nature **393**, 663–665 (1998)
110. Kralchevsky, P.A., Denkov, N.D.: Capillary forces and structuring in layers of colloidal particles. Curr. Opin. Colloid Interface Sci. **6**, 383–401 (2001)
111. Danov, K.D., Pouligny, B., Kralchevsky, P.A.: Capillary forces between colloidal particles confined in a liquid film: the finite-meniscus problem. Langmuir **17**, 6599–6609 (2001)
112. Hurd, A.J., Schaefer, D.W.: Diffusion-limited aggregation in two dimensions. Phys. Rev. Lett. **54**, 1043–1046 (1985)
113. Burmeister, F., Schafle, C., Matthes, T., Bohmisch, M., Boneberg, J., Leiderer, P.: Colloid monolayers as versatile lithographic masks. Langmuir **13**, 2983–2987 (1997)
114. Wickman, H.H., Korley, J.N.: Colloid crystal self-organization and dynamics at air/water interface. Nature **393**, 445–447 (1998)
115. Paunov, V.N., Kralchevsky, P.A., Denkov, N.D., Nagayama, K.: Lateral capillary forces between floating submillimeter particles. J. Colloid Interface Sci. **157**, 100–112 (1993)

116. Dimitrov, A.S., Miwa, T., Nagayama, K.: A comparison between the optical properties of amorphous and crystalline monolayers of silica particles. Langmuir **15**, 5257–5264 (1999)
117. Kralchevsky, P.A., Nagayama, K.: Capillary forces between colloidal particles. Langmuir **10**, 23–26 (1994)
118. Arsenault, A., Fleischhaker, F., von Freymann, G., Kitaev, V., Miguez, H., Mihi, A., Te´treault, N., Vekris, E., Manners, I., Aitchison, S., Perovic, D., Ozin, G.A.: Perfecting imperfection—designer defects in colloidal photonic crystals. Adv. Mater. **18**, 2779–2785 (2006)
119. de Villeneuve, V.W.A., Dullens, R.P.A., Aarts, D.G.A.L., Groeneveld, E., Scherff, J.H., Kegel, W.K., Lekkerkerker, H.N.W.: Colloidal hard-sphere crystal growth frustrated by large spherical impurities. Science **309**, 1231–1233 (2005)
120. Arora, A.K., Tata, B.V.R.: Ordering and Phase Transitions in Colloidal Systems. VCH, Weinheim (1996)
121. Pieranski, P.: Colloidal crystals. Contemp. Phys. **24**, 25–73 (1983)
122. van Negen, W., Shook, I.: Equilibrium properties of suspensions. Adv. Colloid Interface Sci. **21**, 119–194 (1984)
123. Asher, S.A., Flaugh, P.L., Washinger, G.: Crystalline colloidal Bragg diffraction devices: the basis for a new generation of Raman instrumentation. Spectroscopy **1**, 26–31 (1986)
124. Flaugh, P.L., Donnell, S.E.O., Asher, S.A.: Development of a new optical wavelength rejection filter: development of its utility in Raman spectroscopy. Appl. Spectrosc. **38**, 847–850 (1984)
125. Carlson, R.J., Asher, S.A.: Characterization of optical diffraction and crystal structure in monodisperse polystyrene colloids. Appl. Spectrosc. **38**, 297–304 (1984)
126. VanWinkle, D.H., Murray, C.A.: Layering transitions in colloidal crystals as observed by diffraction and direct-lattice imaging. Phys. Rev. A **34**, 562–573 (1986)
127. Pieranski, P., Strzelecki, L., Pansu, B.: Thin colloidal crystals. Phys. Rev. Lett. **50**, 900–903 (1983)
128. Neser, S., Bechinger, C., Leiderer, P., Palberg, T.: Finite-size effects on the closest of hard spheres. Phys. Rev. Lett. **79**, 2348–2351 (1997)
129. Park, S.H., Qin, D., Xia, Y.: Crystallization of meso-scale particles over large areas. Adv. Mater. **10**, 1028–1031 (1998)
130. Park, S.H., Xia, Y.: Crystallization of meso-scale particles over large areas and its application in fabricating tunable optical filters. Langmuir **15**, 266–273 (1999)
131. Park, S.H., Gates, B., Qin, D., Xia, Y.: A three-dimensional photonic crystal operating in the visible. Adv. Mater. **11**, 462–466 (1999)
132. Berthier, S.: Iridescence. The Physical Colours of Insets. Springer (2007)
133. Fox, D.L.: Animal Biochromes and Structural Colors. University of California, Berkely (1976)
134. Ghiradella, H.: Light and color on the wing—structural colors in butterflies and moths. Appl. Opt. **30**, 3492–3500 (1991)
135. Kinoshita, S., Yoshioka, S., Miyazaki, J.: Physics of structural colors. Rep. Prog. Phys. **71**, 076401 (2008)
136. Parker, A.R.: 515 million years of structural color. J. Opt. A Pure Appl. Opt. **2**, R15–R28 (2000)
137. Parker, A.R.: Bird Coloration, vol. 1. Mechanism and Measurements, vol 2. Function and Evolution. Tls-Times Lit Suppl, 4–4 (2006)
138. Srinivasarao, M.: Nano-optics in the biological world: beetles, butterflies, birds, and moths. Chem. Rev. **99**, 1935–1961 (1999)
139. Vukusic, P., Sambles, J.R.: Photonic structures in biology. Nature **424**, 852–855 (2003)
140. Li, Y.Z., et al.: Structural origin of the brown color of barbules in male peacock tail feathers. Phys. Rev. E **72**, 010902 (2005)
141. Vukusic, P., Sambles, J.R., Lawrence, C.R.: Structural color—color mixing in wing scales of a butterfly. Nature **404**, 457–457 (2000)
142. Vukusic, P., Sambles, R., Lawrence, C., Wakely, G.: Sculpted-multilayer optical effects in two species of Papilio butterfly. Appl. Opt. **40**, 1116–1125 (2001)

143. Wong, T.H., Gupta, M.C., Robins, B., Levendusky, T.L.: Color generation in butterfly wings and fabrication of such structures. Opt. Lett. **28**, 2342–2344 (2003)
144. Zi, J., et al.: Coloration strategies in peacock feathers. Proc. Natl. Acad. Sci. U.S.A. **100**, 12576–12578 (2003)
145. Liu, F., Dong, B.Q., Liu, X.H., Zheng, Y.M., Zi, J.: Structural color change in longhorn beetles Tmesisternus isabellae. Opt. Express **17**, 16183–16191 (2009)
146. Vukusic, P.: Evolutionary photonics with a twist. Science **325**, 398–399 (2009)
147. Liu, F., et al.: Inconspicuous structural coloration in the elytra of beetles Chlorophila obscuripennis (Coleoptera). Phys. Rev. E **77**, 012901 (2008)
148. Kinoshita, S.: Structural Colors in the Realm of Nature. World Scientific Publishing Co., Singapore (2008)
149. Chen, Y., Gu, J.J., Zhu, S.M., Fan, T.X., Zhang, D., Guo, Q.X.: Iridescent large-area $ZrO_2$ photonic crystals using butterfly as templates. Appl. Phys. Lett. **94**, 053901 (2009)
150. Ge, H.L., Song, Y.L., Jiang, L., Zhu, D.B.: One-step preparation of polystyrene colloidal crystal films with structural colors and high hydrophobicity. Thin Solid Films **515**, 1539–1543 (2006)
151. Wang, J.X., Wen, Y.Q., Ge, H.L., Sun, Z.W., Zheng, Y.M., Song, Y.L., Jiang, L.: Simple fabrication of full color colloidal crystal films with tough mechanical strength. Macromol. Chem. Phys. **207**, 596–604 (2006)
152. You, B., Wen, N.G., Shi, L., Wu, L.M., Zi, J.: Facile fabrication of a three-dimensional colloidal crystal film with large-area and robust mechanical properties. J. Mater. Chem. **2009**(19), 3594–3597 (2009)
153. Wang, J.X., Wen, Y.Q., Hu, J.P., Song, Y.L., Jiang, L.: Fine control of the wettability transition temperature of colloidal-crystal films: from superhydrophilic to superhydrophobic. Adv. Funct. Mater. **17**, 219–225 (2007)
154. Wang, J.X., Wen, Y.Q., Hu, J.P., Song, Y.L., Jiang, L.: Control over the wettability of colloidal crystal films by assembly temperature. Macromol. Rapid Commun. **27**, 188–192 (2006)
155. Wang, J.X., Wen, Y.Q., Hu, J.P., Song, Y.L., Jiang, L.: Bioinspired colloidal photonic crystals with controllable wettability. Acc. Chem. Res. **44**, 405–415 (2011)
156. Fudouzi, H., Xia, Y.N.: Colloidal crystals with tunable colors and their use as photonic papers. Langmuir **19**, 9653–9660 (2003)
157. Sato, O., Kubo, S., Gu, Z.Z.: Structural color films with lotus effects, superhydrophilicity, and tunable stop-bands. Acc. Chem. Res. **42**, 1–10 (2009)
158. Liu, X.Y., Diao, Y.Y.: Light reflective structures and methods for their manufacture and use. PCT/SG2011/000075 (2011)
159. Velev, O.D., Kaler, E.W.: Structured porous materials via colloidal crystal templating: from inorganic oxides to metals. Adv. Mater. **12**, 531–534 (2000)
160. Holland, B.T., Blanford, C.F., Do, T., Stein, A.: Synthesis of highly ordered, three-dimensional, macroporous structures of amorphous or crystalline inorganic oxides, phosphates, and hybrid composites. Chem. Mater. **11**, 795–805 (1999)
161. Holland, B.T., Blanford, C.F., Stein, A.: Synthesis of macroporous minerals with highly ordered three-dimensional arrays of spheroidal voids. Science **281**, 538–540 (1998)
162. Holland, B.T., Abrams, L., Stein, A.: Dual templating of macroporous silicates with zeolitic microporous frameworks. J. Am. Chem. Soc. **121**, 4308–4309 (1999)
163. Johnson, S.A., Ollivier, P.J., Mallouk, T.E.: Ordered mesoporous polymers of tunable pore size from colloidal silica templates. Science **283**, 963–965 (1999)
164. Wang, J.X., Zhang, Y.Z., Wang, S.T., Song, Y.L., Jiang, L.: Bioinspired colloidal photonic crystals with controllable wettability. Acc. Chem. Res. **44**, 405–415 (2011)
165. Ge, J., Yin, Y.: Responsive photonic crystals. Angew. Chem. Int. Ed. **50**, 1492–1522 (2011)
166. Ge, J., Hu, Y., Yin, Y.: Highly tunable superparamagnetic colloidal photonic crystals. Angew. Chem. **119**, 7572–7575 (2007)
167. Saito, H., Takeoka, Y., Watanabe, M.: Simple and precision design of porous gel as a visible indicator for ionic species and concentration. Chem. Commun. 2126–2127 (2003)

168. Takeoka, Y., Watanabe, M.: Tuning structural color changes of porous thermosensitive gels through quantitative adjustment of the cross-linker in pre-gel solutions. Langmuir **19**, 9104–9106 (2003)
169. Sharma, A.C., Jana, T., Kesavamoorthy, R., Shi, L.J., Virji, M.A., Finegold, D.N., Asher, S.A.: A general photonic crystal sensing motif: creatinine in bodily fluids. J. Am. Chem. Soc. **2004**(126), 2971–2977 (2004)
170. Puzzo, D.P., Arsenault, A.C., Manners, I., Ozin, G.A.: Electroactive inverse opal: a single material for all colors. Angew. Chem. Int. Ed. **48**, 943–947 (2009)
171. Ozaki, M., Shimoda, Y., Kasano, M., Yoshino, K.: Electric field tuning of the stop band in a liquid-crystal-infiltrated polymer inverse opal. Adv. Mater. **14**, 514–518 (2002)
172. Kolle, M., Salgard-Cunha, P.M., Scherer, M.R.J., Huang, F.M., Vukusic, P., Mahajan, S., Baumberg, J.J., Steiner, U.: Mimicking the colourful wing scale structure of the Papilio blumei butterfly. Nat. Nanotechnol. **5**, 511–515 (2010)
173. Diao, Y.Y., Liu, X.Y.: Mysterious coloring: structural origin of color mixing for two breeds of Papilio butterflies. Opt. Express **2011**(19), 9232–9241 (2011)
174. Lim, M.L.M., Land, M.F., Li, D.Q.: Sex-specific UV and fluorescence signals in jumping spiders. Science **315**, 481 (2007)
175. Briscoe, A.D., Bybee, S.M., Bernard, G.D., Yuan, F.R., Sison-Mangus, M.P., Reed, R.D., Warren, A.D., Llorente-Bousquets, J., Chiao, C.C.: Reply to Nozawa et al. Complementary statistical methods support positive selection of a duplicated UV opsin gene in Heliconius. Proc. Natl. Acad. Sci. **107**, 3628–3633 (2010)
176. Takeuchi, Y., Arikawa, K., Kinoshita, M.: Color discrimination at the spatial resolution limit in a swallowtail butterfly, Papilio xuthus. J. Exp. Biol. **209**, 2873–2879 (2006)
177. Bartlett, P.N., Birkin, P.R., Ghanem, M.A.: Electrochemical deposition of macroporous platinum, palladium and cobalt films using polystyrene latex sphere templates. Chem. Commun. **17**, 1671–1672 (2001)
178. Braun, P.V., Wiltzius, P.C.O.: Macroporous materials—electrochemically grown photonic crystals. Curr. Opin. Colloid Interface Sci. **7**, 116–123 (2002)
179. Wijnhoven, J.E.G.J., Zevenhuizen, S.J.M., Hendriks, M.A., Vanmaekelbergh, D., Kelly, J.J., Vos, W.L.: Electrochemical assembly of ordered macropores in gold. Adv. Mater. **12**, 888–890 (2000)
180. Puurunen, R.L.: Surface chemistry of atomic layer deposition: a case study for the trimethylaluminum/water process. J. Appl. Phys. **97**, 121301 (2005)
181. Labhart, T., Baumann, F., Bernard, G.D.: Specialized ommatidia of the polarization-sensitive dorsal rim area in the eye of monarch butterflies have non-functional reflecting tapeta. Cell Tissue Res. **338**, 391–400 (2009)